Study of Micro-High Speed Bearings and Rotor Dynamics for Micromachine Gas Turbines

Kousuke Isomura
Ishikawajima-Harima Heavy Industries Co., Ltd.
3-5-1 Mukodai-cho Nishi-Tokyo-shi
Tokyo 188-8555
JAPAN

Kousuke_isomura@ihi.co.jp

Shin-ichi Togo
Tohoku-Gakuin University
13-1 Chuo 1-chome
Tagajo-shi 985-8537
JAPAN

Shuji Tanaka
Tohoku University
Aza-Aoba 01, Aramaki Aoba-ku
Sendai-shi 980-8579
JAPAN

ACKNOWLEDGEMENT

The basic research on high-speed gas bearings has been supported by The Asian Office of Aerospace Research and Development (AOARD), grant number F62562-03-T-0452, program manager Dr. Brett Pokines.

ABSTRACT

Micromachine gas turbines require extremely high rotor speed to realize the same impeller tip speed to the large gas turbines, by very small diameter of the impellers. Hence, the rotordynamics is one of the critical issues. Especially, the bearing speed will exceed the range of experience in any existing turbomachines, and hence the method to achieve the stable operation at the required design speed has not established, yet. The characteristics of variety of bearings will be reviewed, and the issues of the bearing selection and the rotordynamic design will be addressed.

1.0 INTRODUCTION

1.1 New Markets for Micromachine Gas Turbine Generators

Recent advances in autonomous robots are causing increase of power requirements. Robots are expanding their capability of complicated movement, and developers are trying to add a lot of new functions to a robot, such as playing trumpet for example. These new functions use more servomotors that increase the total power requirement of a robot. So far, almost all robots use batteries for their power source. Lithium Ion batteries and Nickel-Metal Hydride batteries are the major types of batteries currently used in robots. Battery is well known as a high power density electric source. It is a good power source for applications as robots that require large current to power many servomotors. However, battery has a weakness of low energy density. The continuous operation time is short. These day's autonomous robots can operate only 30 minutes after half a day of battery recharging. This short operation time will largely limit the application of autonomous robots. A lot of technology improvements have already been achieved over decades for batteries, and the room for large performance improvement is becoming small, now.

Isomura, K.; Togo, S.-I.; Tanaka, S. (2005) Study of Micro-High Speed Bearings and Rotor Dynamics for Micromachine Gas Turbines. In *Micro Gas Turbines* (pp. 7-1 – 7-62). Educational Notes RTO-EN-AVT-131, Paper 7. Neuilly-sur-Seine, France: RTO. Available from: http://www.rto.nato.int/abstracts.asp.

Therefore, increase of the operation time by battery power will result in the increase of battery weight, which will in turn cause an increase of the power requirement. This will cause further increase of the battery weight, and the system weight increases by snowball effect.

To increase the energy density to achieve long operation time, some people is expecting the development of fuel cells. Fuel cell is known for its high energy density and high thermal efficiency. However, it should be noted that the power density of the fuel cell is low unless otherwise the current density is increased by paying the cost of efficiency drop. It suits to power applications that require high voltage with small current, but it does not suit to power electric motors.

Power sources that have both high power density and high energy density are internal combustion engines. Among variety of internal combustion engines, the type suits for the micro-size generator would be the continuous combustion type and continuous rotation type without any rubbing seal. Surface roughness, and therefore the friction loss will become relatively large at micro-scale. In addition, intermittent combustion will become difficult at micro-scale because the heat loss through the surface becomes relatively large. Hence, gas turbine is expected to be a suitable power source for a generator at micro-scale. The target cycle of the 100W class micromachine gas turbine generator is shown in Figure 1-1.

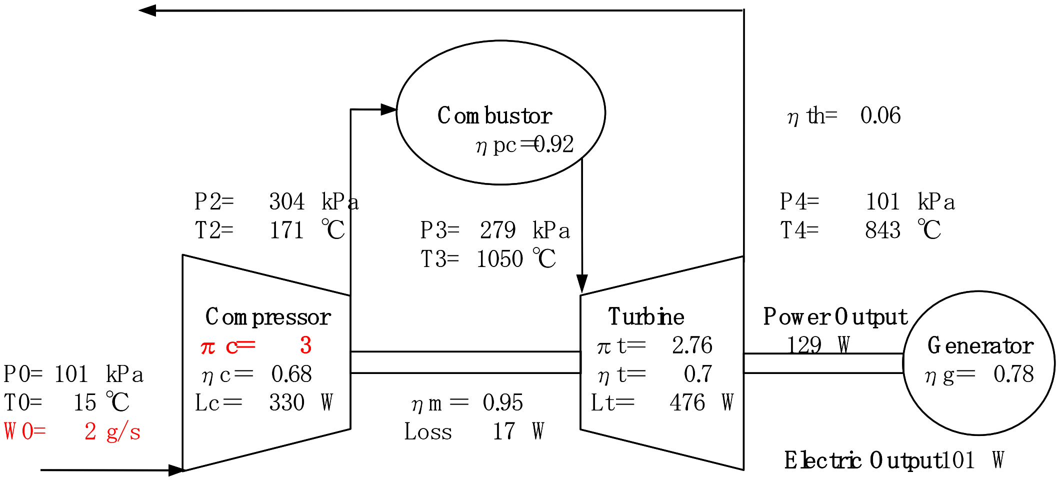

Figure 1-1: The Target Cycle for 100W Gas Turbine Generator.

1.2 Needs for High-Speed Micro-Gas Bearings in Micromachine Gas Turbines

The rotor speed of gas turbine is defined by the required pressure ratio of the compressor. The required compressor pressure ratio is found from the cycle study. In the cycle of 100W micromachine gas turbine shown in Figure 1-1, the compressor is expected to generate pressure ratio 3. From the pressure ratio, the required impeller tip tangential speed is calculated. Since the tangential speed is a product of the rotational speed and the impeller diameter, the rotational speed becomes inversely proportional to the rotor diameter. Hence, the shaft speed increases as the impeller diameter reduces. This relation for pressure ratio 3 is shown in Figure 1-2. For current impeller of diameter 10mm, the required shaft speed is found to be 870,000 rpm.

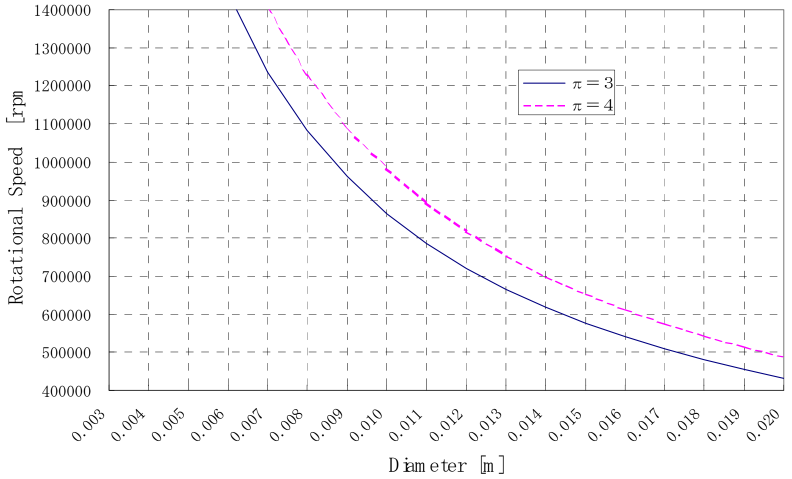

Figure 1-2: Relation of the Impeller Diameter and the Rotational Speed.

The key component to realize this shaft speed is the bearings. The common measure of the performance of ball bearings is a DN number, which is a product of diameter D in mm, and shaft speed N in rpm. If we use a shaft of diameter 4mm to support this rotor, which looks to be about the smallest limit to support 10mm diameter impellers, the DN number becomes 3,480,000. This number is beyond that of currently available bearings for practical use. This DN number is about the champion data in laboratory environment of bearing test rig with excessive amount of lubrication oil. For the practical use, DN number around 2,000,000 would be a reasonable limit, if long life is required. For 4mm shaft, it is 500,000 rpm. If we limit the selection of bearing as ball bearings, which are the most matured and reliable bearing of these days, we have to reduce the shaft speed. The reduction of the shaft speed will require the increase of the impeller diameter to achieve the same pressure ratio. Since the centrifugal compressor impellers have the range of exit blade height to diameter ratio to operate at reasonable adiabatic efficiency (Figure 1-3), the efficiency will be penalized to keep the same output power when the impeller diameter increases. If we keep the exit blade height to diameter ratio about the same, it will result in the increase of the mass flow rate, and hence in the increase of the output power. Therefore, a very high shaft speed is required, and high speed bearings are essential for realizing very small gas turbines. An alternative to ball bearing has to be developed for the shaft speed over 500,000 rpm.

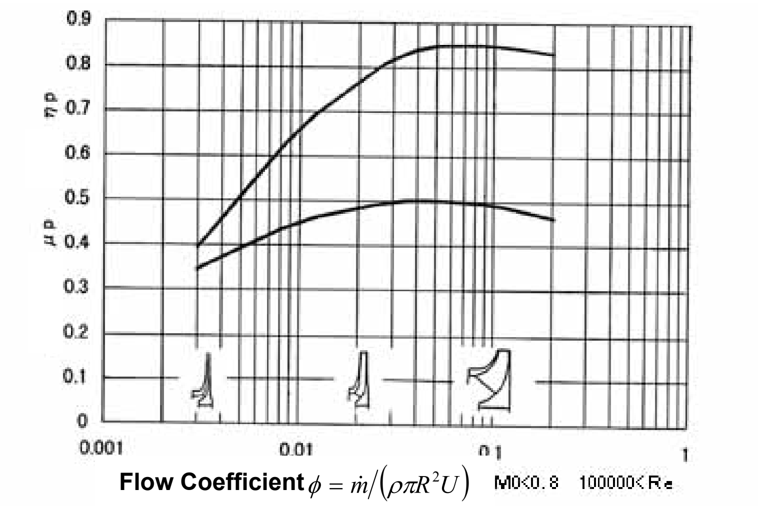

Figure 1-3: Exit Blade Height and the Adiabatic Efficiency of Centrifugal Compressors.

2.0 REQUIREMENTS

2.1 Load Capacity

In any high-speed rotating machines, the over loading of the bearings will cause fatal results. The bearings will be burnt by the heat generated by the friction, and the rotor shaft will stick to the bearings. Hence, it is very important to assess the load capacity of the bearing accurately to design the bearing that the load will never exceed the load capacity of the bearing. In the mobile gas turbine, it is also very important and difficult to assess the maximum loading that the bearings will experience during the all possible operation. For example, the jet engines of fighter aircrafts will operate under various maneuvers. It will encounter the largest load at the hard landing to the carrier. Hence, the requirement for the bearings of fighter engines usually specifies to sustain about 9G of the load.

In palm-top gas turbines, one source of the large load will be the gyro moment during the rapid and random change of the orientation. However, similar to the jet engines, the largest load will probably be encountered when it is dropped to the hard floor during the operation. Even from just a couple of meters of the height, the maximum load at the instance of the impact will be significantly larger than 9G. In high-speed rotating machines, even a short time of overloading can be fatal, and hence, should be avoided. Hence, the bearing should be designed to sustain about 50G of the load, for the first design, until the real requirements is verified by dropping tests in the real products.

2.2 Requirements on Passing through the Resonance Frequencies

As shown in Figure 2-1, gas turbines usually operate above the first two resonance speed. Those are the two rigid mode vibrations; i.e. conical mode and cylindrical mode. Which mode has lower frequency depends on the configuration of the rotor. For a shaft with mass on the both end, the conical mode frequency is usually lower. Sometimes, the rotor is designed to have both the compressor and the turbine at one end of the rotor, to make the assembling easy. In such a case, the engine operation speed may be higher than the third mode, which is often called as supercritical operation. In any case, the rotor should be able to pass through the resonance speed without too much of rotor vibration amplitude to damage the bearings.

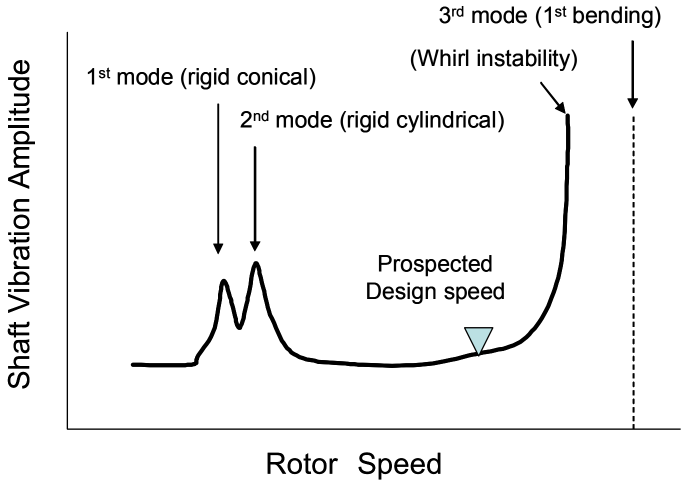

Figure 2-1: Instability around the Design Speed of the Micro-Rotor.

Also, the operation speed should be sufficiently apart from the first three resonance speeds. The operation speed is usually set to have more than 50% of the frequency margin to the resonance speed, which means that the difference between the resonance speed and the operation speed is larger than 50% of the operation speed, if the robustness is required.

2.3 Power Loss

The power loss of the bearing is better the lower. The cycle calculation results in Figure 1-1 shows a guideline, although it is not an absolute requirement. There are rooms for trade-off between the component performances.

One thing to be noted is that as a mobile power system, the advantage should be evaluated as the whole closed system. The power loss should be compared including both the loss in the bearings and the power required to pump the lubricant.

2.4 Stability Requirements at High Speed

If ball bearings are used, then the maximum bearing speed is limited by the skidding due to the break down of the lubrication oil film. If gas bearings are used, it is limited by the whirl instability. Whirl is the rotating instability of the rotor shaft caused by the dynamic gas force effect in the bearing gap that works in orthogonal direction to the motion of the center of the rotor. The gas bearings are required not to show any whirl instability at the design rotor speed.

3.0 SELECTION OF THE BEARINGS

3.1 Various Types of Bearings

There are several different candidates for the bearings suitable for high-speed operation in very small gas turbines. Those are ceramic ball bearings, magnetic bearings and gas bearings, and there are various types of gas bearings. The merit and demerit of each type of bearing are tabulated in Table 3-1.

Table 3-1: Merit and Demerit of Various Types of Bearings (continued on next page)

Bearing Type	Merit	Demerit
Ball Bearings	Very large load capacity	Needs oil to lubricate Speed limited by DN=2,500,000
Magnetic Bearing	Low viscous loss	Heavy and bulky Magnet requires low temperature
Foil Bearing	Works at high temperature Absorbs heat expansion No need for external power Large damping High stability	Difficult to design
Tilting Pad Bearing	Very high stability	Difficult to fabricate
Lobe Bearing	Easy to fabricate High stability No need for external power	Large viscous loss
Herringbone Bearing	High stability Design method exists No need for external power	Needs high accuracy Low damping Large viscous loss

Bearing Type	Merit	Demerit
Squeeze Film Bearings		Needs external power to generate the squeezing vibration Still under development
Static Gas Bearing	High loading capacity Wide bearing gap	Needs supply air Low whirl limit (whirl ratio=2)
Hydroinertia Gas Bearing	High loading capacity High whirl stability Very wide bearing gap (low accuracy requirement)	Needs large volume of supply air Not much known

The maximum speed of the ball bearings is limited by skidding. In ball bearings, the ball and the shaft is supposed not to skid. At high speed, the increase of the drag between the ball and the retainer increases, and the balls start to skid The common measure of the maximum speed of ball bearings is a DN number, which is a product of diameter D in mm, and shaft speed N in rpm. If we use a shaft of diameter 4mm to support this rotor, which looks to be about the smallest limit to support 10mm diameter impellers, the DN number becomes 3,480,000. This number is beyond that of currently available bearings for practical use. This DN number is about the champion data in laboratory environment of bearing test rig with excessive amount of lubrication oil. For the practical use, DN number around 2,500,000 would be a reasonable limit, if long life is required. For 4mm shaft, it is about 600,000 rpm. If we limit the selection of bearing as ball bearings, which are the most matured and reliable bearing of these days, we have to reduce the shaft speed. The reduction of the shaft speed will require the increase of the impeller diameter to achieve the same pressure ratio. Since the centrifugal compressor impellers have the range of exit blade height to diameter ratio to operate at reasonable adiabatic efficiency (Figure 1-3), the efficiency will be penalized to keep the same output power when the impeller diameter increases. If we keep the exit blade height to diameter ratio about the same, it will result in the increase of the mass flow rate, and hence in the increase of the output power. Therefore, a very high shaft speed is required, and high speed bearings are essential for realizing very small gas turbines. An alternative to ball bearing has to be developed for the shaft speed over 600,000 rpm.

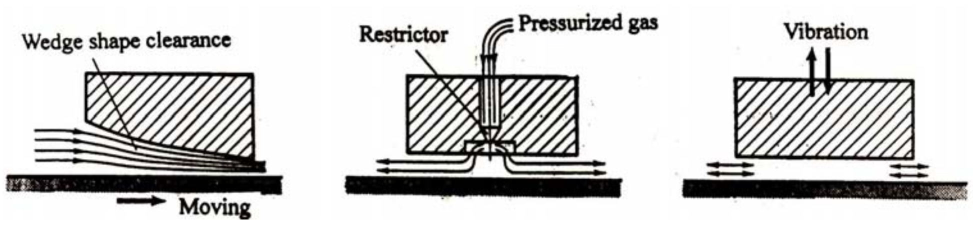

(a) Hydrodynamic type (b) Hydrostatic type (c) Squeeze type

Figure 3-1: Working Principle of Conventional Gas Bearings.

The magnetic bearing has a demerit with the low temperature requirement. The magnetic force drops drastically at the temperature over the Curie Point, while in a very small gas turbine, it is difficult to shield the heat from the combustor and the turbine, so the temperature of the bearing can become very high.

In general, gas bearings have capability of operating under high temperature environment. There are mainly three types of gas bearings. They are Hydrodynamic type (Self-acting gas bearings), Hydrostatic type (Externally pressurized gas bearings) and Squeeze type (Squeeze film gas bearings). Figure 3-1 shows the working principle of these gas bearings. In hydrodynamic type, load is supported by pressure generated by the wedge action. Gas is drawn into the wedge shaped gap by the relative motion of the surfaces according to its viscosity and is compressed. In hydrostatic type, load is supported by the static pressure of the pressurized feeding gas. In squeeze type, two surfaces are vibrating perpendicular to the surfaces with high frequency and the gas in the gap is trapped according to its viscosity and is compressed. The pressure distribution in the bearing clearances of hydrodynamic journal bearing and hydrostatic journal bearing are shown in Figure 3-2.

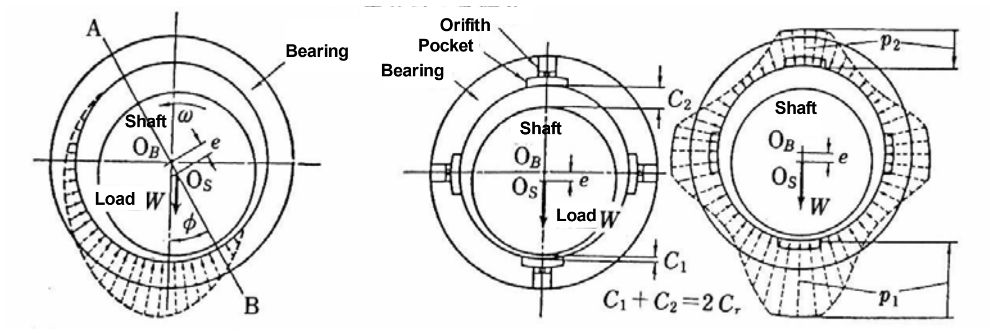

(a) Hydrodynamic gas bearing **(b) Hydrostatic gas bearing**

Figure 3-2: Pressure Distribution in the Bearing Clearance of Journal Bearings.

Working principle of these three types of gas bearings are different but they have one in common. The bearing clearance is very small compared with their dimensions. The bearing clearance is usually in order of less than 1/1000 of the bearing dimensions. Consequently, flow of the gas in the bearing clearance is governed mainly by the viscous effect and the inertia effect of the gas is usually neglected. If the bearing clearance becomes large, hydrodynamic type and squeeze type cannot generate enough aerodynamic force to keep the shaft floated because the viscous effect of the gas flow in the bearing clearance becomes weak. In such case, only the hydrostatic type of the gas bearing works. Hence, among the various gas bearings, hydrostatic types usually have larger bearing clearance than the other types.

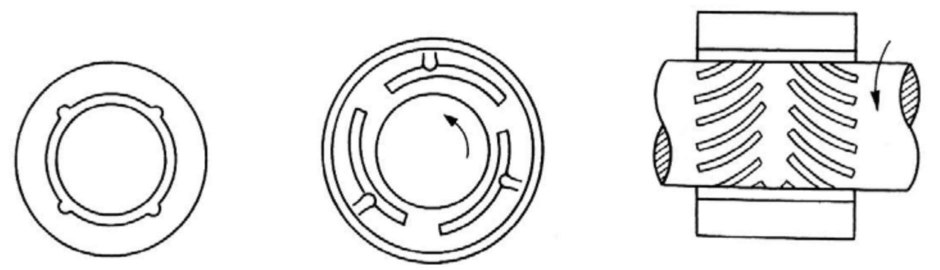

(a) Lobe bearing **(b) Tilting pad bearing** **(c) Herring-bone bearings**

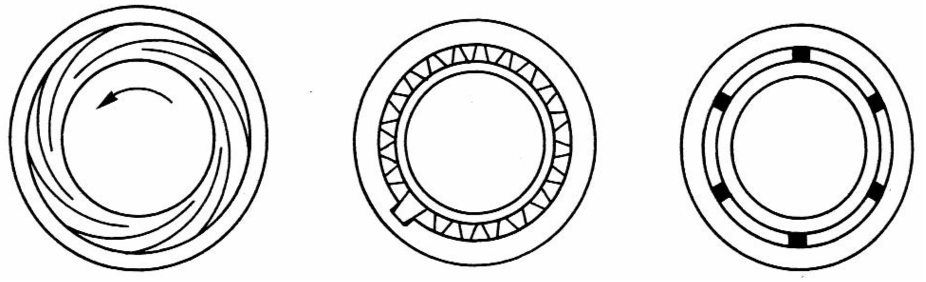

(d) Foil Bearings

Figure 3-3: Variety of Hydrodynamic Journal Bearings.

The hydrodynamic gas bearings, such as foil bearings, tilting pad bearings, lobe bearings, and Herring-bone bearings, have an advantage that they don't need external power to supply the bearing gas, but they require fabrication technology or skills to fabricate the parts at extremely high accuracy to realize the bearing clearance smaller than 10μm. The hydrostatic gas bearings have advantages that they require less accuracy for the fabrication than hydrodynamic gas bearings because their bearing clearance is larger than 10μm, and that the load capacity is large from the low shaft speed and that the load capacity and the stiffness are independently controllable. These advantages will make this type of bearings relatively easy to start running. However, hydrostatic gas bearings have a fatal disadvantage that the whirl instability limit is rather low. The whirl ratio, which is the rotational speed divided by whirl speed at the stability limit, is shown to be 2 by classical analysis with incompressible flow assumption, hence the maximum rotor speed cannot go beyond twice the resonance speed.

Hydroinertia gas bearings are a type of hydrostatic gas bearings that have a bearing clearance larger than the usual hydrostatic gas bearings, so the flow in the bearing clearance becomes compressible supersonic flow. It is known for the high whirl stability at very high speed. The whirl ratio can become more than 10, due to the compressibility effect of the supersonic flow in the bearing clearance. The advantage of less strict requirements for the fabrication accuracy is even better than usual hydrostatic gas bearings. The disadvantage of this bearing is that the bearing consumes relatively large amount of bearing supply gas.

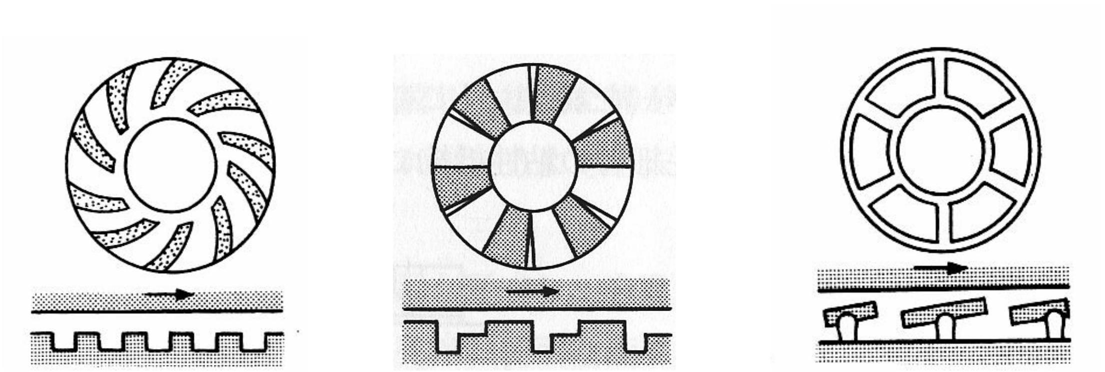

(a) Spiral grooves **(b) Step grooves** **(c) Tilting pad**

Figure 3-4: Variety of Hydrodynamic Thrust Bearings.

After comparing various bearings, following assessments are made.

(1) Ball bearings can be used if the required power increases and the design speed comes lower than 600,000 rpm, or if the technology improves and bearings that can operate at the design speed comes into market. Although the treatment of the lubrication oil under the heated environment is an issue to be resolved.

(2) The hydrodynamic gas bearings, such as foil bearings, Herring-bone & spiral groove bearings and lobe bearings will be the best candidate for the bearings for micromachine gas turbines.

(3) Hydroinertia gas bearings have a potential to achieve the current design speed of 870,000 rpm, in the shortest development period. Hence, it will be a good choice to use them for the initial phase of the development to accelerate the development of the compressors.

3.2 Hydroinertia Gas Bearings

3.2.1 Definition of Hydroinertia Gas Bearings

For the hydrostatic gas bearings with large bearing clearance, inertia effect of the gas flow in the bearing clearance becomes predominant and its Mach number exceeds 1. As the results, gauge pressure in the bearing clearance becomes negative. Figure 3-5 shows an example of Mach number and pressure distribution of a circular thrust gas bearing with large bearing clearance. Such hydrostatic gas bearings are called "*Hydroinertia gas bearing*"contrasted with the conventional hydrostatic gas bearings with small bearing clearance. It is defined as a kind of hydrostatic gas bearings (externally pressurized gas bearings) with large bearing clearance that the gas flow in the bearing clearance is governed by inertia effect.

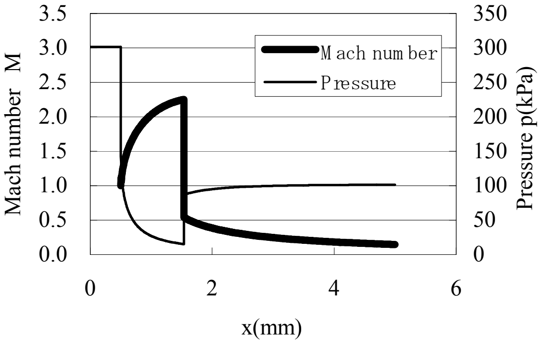

Figure 3-5: Distribution of Mach Number and Pressure of a Circular Thrust Bearing.

3.2.2 Negative Pressure in Bearing Clearance

In conventional hydrostatic gas bearings, load capacity increases with increase in supply pressure. But in hydroinertia gas bearings, increase in supply pressure may cause decrease in load capacity. As the load capacity is the sum of the pressure distribution in bearing clearance, the decrease in load capacity is caused by "unusual" phenomenon in pressure distribution.

To explain the "unusual" phenomenon in pressure distribution, a simple circular thrust gas bearing with a supply hole at the center shown in Figure 3-6 is taken as an example.

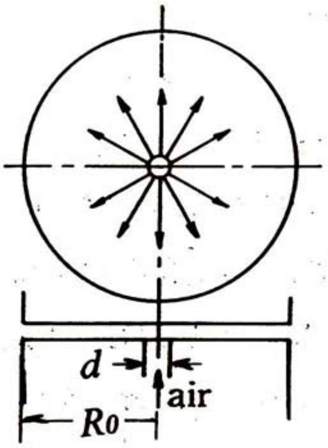

Figure 3-6: Circular Trust Gas Bearing.

Figure 3-7 shows an example of the "unusual" phenomena in pressure distribution of a hydroinertia gas bearing [1]. As shown in the figure, negative pressure is generated in the bearing clearance. And the area of the negative pressure area at high supply pressure is wider than that of low supply pressure. This causes decrease in load capacity at high supply pressure. This unusual phenomenon was found fairly early [2]. And up to present, hydroinertia gas bearings have been thought as unpractical and useless bearings.

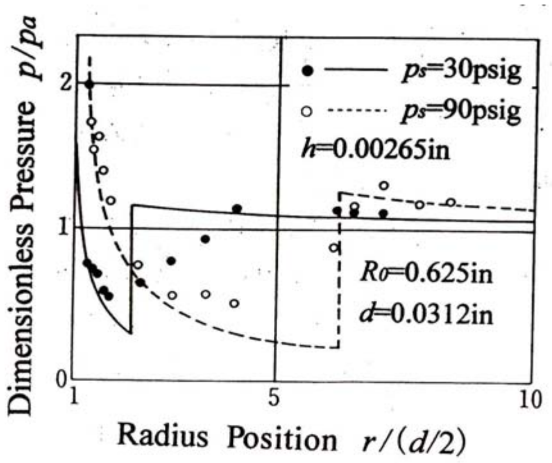

Figure 3-7: Pressure Distribution of a Circular Thrust Hydroinertia Gas Bearing.

The mechanism of this unusual phenomena is explained by the flow model shown by Figure 3-8. In the figure, air is supplied through the center hole with supply pressure of p_s. At the exit of the center hole, pressure decreases to p_0 by the inherent orifice effect. When the bearing clearance h is small, reduction of the pressure at the exit of the center hole is small and the pressure distribution in the bearing clearance becomes pure viscous type as shown by dotted line in the figure. Flow speed u of the air in the bearing clearance does not exceed sonic velocity a. This is the case of conventional hydrostatic gas bearings, and the load capacity increases with increase in supply pressure.

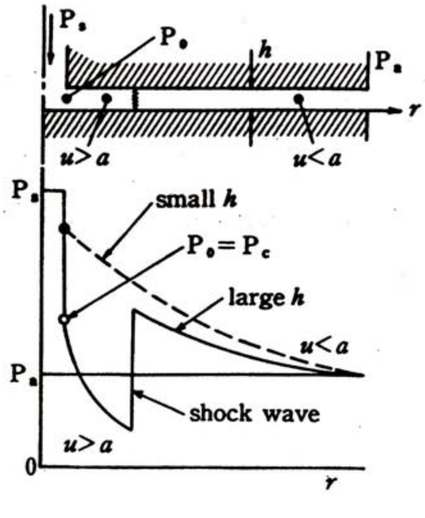

Figure 3-8: Flow Model of Hydroinertia Circular Thrust Gas Bearing.

In case of large bearing clearance, the pressure p_0 at the exit of the center hole reduces to the critical pressure, and the flow speed becomes sonic velocity. The exit of the center hole corresponds to the throat and then it flows into the bearing clearance with super sonic velocity and the gauge pressure goes down to negative. The pattern of this super sonic flow is similar to the flow in Laval nozzle. And then, with shock wave, the flow speed drops to subsonic, and the pressure recovers. After that, the flow in the bearing clearance is governed by viscous force and the pressure in the bearing clearance decreases gradually to the ambient pressure.

3.2.3 Characteristics of Hydroinertia Gas Bearings

Figure 3-9 shows the comparison of a conventional hydrostatic circular thrust gas bearing and a hydroinertia circular thrust gas bearing. In a conventional hydrostatic thrust gas bearing, the load is supported by a repulsive force caused by positive pressure. In hydroinertia thrust gas bearings, repulsive force is largely decreased by negative pressure and load capacity is much smaller than that of a conventional gas bearing. Consequently, hydroinertia gas bearings have been thought to be useless. But as shown in the figure, the load can be supported by suction force caused by the negative pressure.

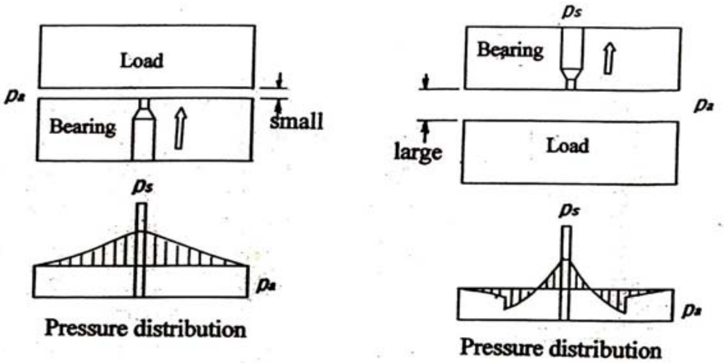

(a) Hydrostatic gas bearing **(b) Hydroinertia gas bearing**

Figure 3-9: A Conventional Hydrostatic Bearing and a Hydroinertia Gas Bearing.

Figure 3-10 shows the load capacity W and volumetric flow rate Q of a hydroinertia circular thrust gas bearing. The load capacity decreases with increase in bearing clearance and it becomes negative when the bearing clearance exceeds 0.07mm. This means that the load capacity is generated by suction force. At over 0.1mm of the bearing clearance, the load capacity becomes almost constant and the bearing stiffness k becomes almost 0. The flow rate increases proportional to the bearing clearance. This means that the flow is choked at the exit of the supply hole.

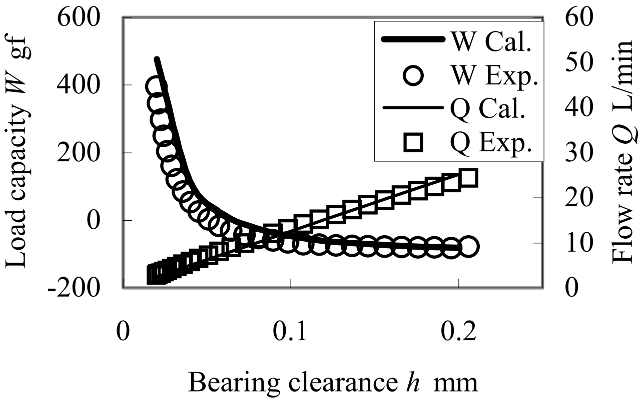

Figure 3-10: Load Capacity and Flow Rate of a Hydroinertia Circular Thrust Gas Bearing (R_0=5mm, d=1mm, p_s=400kPa(abs)).

The fact that the load can be supported by suction force brings an advantage in the case of radial bearings. Figure 3-11 shows the comparison of a conventional hydrostatic radial gas bearing and a hydroinertia radial gas bearing in eccentric condition. In conventional hydrostatic radial gas bearings, the load is supported by the difference of repulsive forces of the large clearance side and of the small clearance side. In hydroinertia radial gas bearing, the load capacity is the sum of the repulsive force of the small clearance side and the suction force of the large clearance side. This makes large load capacity compared with conventional hydrostatic radial bearings.

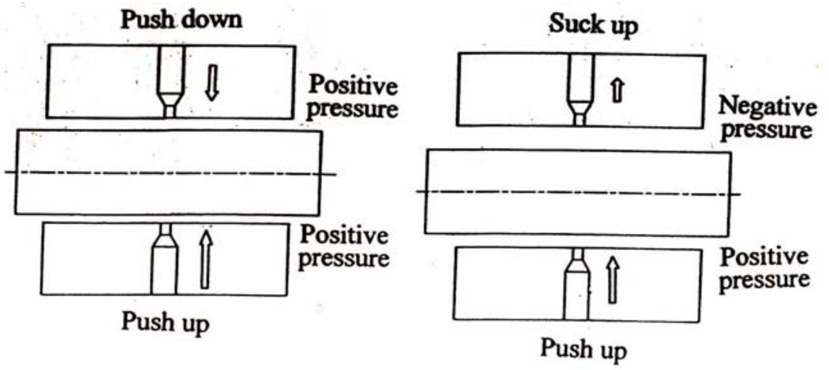

(a) Hydrostatic radial gas bearing (b) Hydroinertia radial gas bearing

Figure 3-11: Comparison of a Hydrostatic Radial Gas Bearing a Hydroinertia Radial Gas Bearing.

Recently, hydroinertia gas bearings are successfully used in ultra high-speed micro spinners. They are applied to a micro spinner for solid Nuclear Magnetic Resonance (NMR) detector [3]. Figure 3-12 shows the construction of the micro spinner. This micro spinner is 4mm in diameter and is supported by hydroinertia gas bearings.

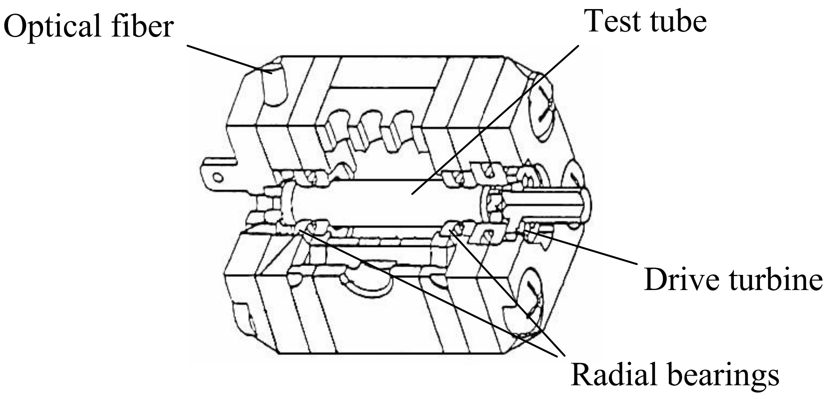

Figure 3-12: Construction of a Solid NMR Detector.

Figure 3-13 shows the relation of rotational speed and the supply pressure to the drive turbine. The micro-spinner stably operated at the rotational speed over 20krps, and it reached the maximum rotational speed reached 21.5krps (=1,290,000rpm).

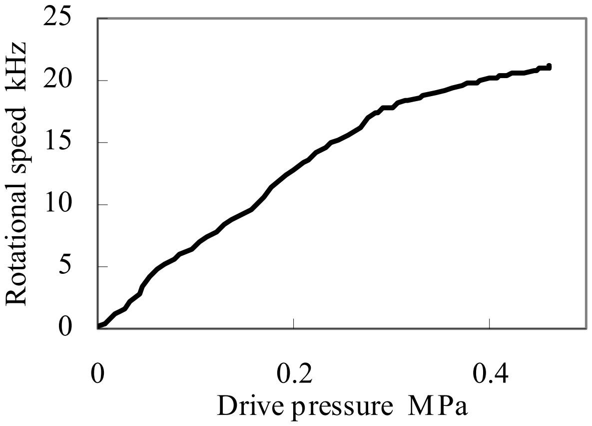

Figure 3-13: Rotational Speed and Turbine Drive Pressure.

The waveforms of the spinner vibration at the rotational speed of 10krps and 20krps are shown in Figure 3-14. In addition to the synchronous vibration, whirl vibrations of the frequency at about 1kHz are clearly seen. It means that the whirl ratio, which is the ratio of the shaft speed to whirl frequency, exceeds 20. At the rotational speed of 20krps, the amplitude of the whirl vibration fluctuates slightly but it does not diverge. The maximum total amplitude of the vibration is about 2.9μm. Since the total bearing clearance is 62μm (mean of the measured values), there are enough margins to the crash.

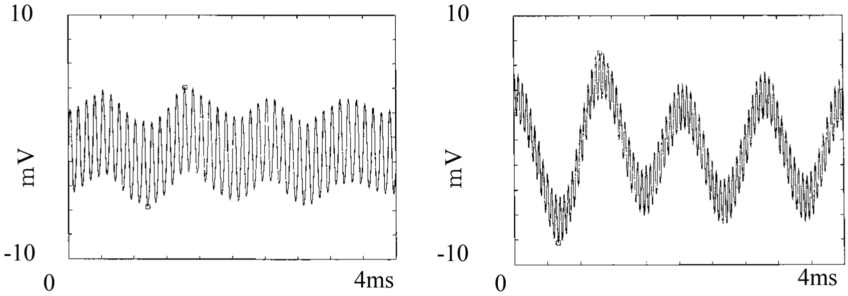

(a) 10krps **(b) 20krps**

Figure 3-14: Wave Forms of the Spinner Vibration.

Figure 3-15 shows the step response of a hydroinertia thrust gas bearing and a conventional hydrostatic gas bearing. Evidently, damping ratio of the hydroinertia gas bearing is much higher than that of conventional hydrostatic gas bearing. The logarithmic damping ratio δ calculated from these step responses, δ=0.1586 for the hydroinertia thrust gas bearing and δ=0.0339 for conventional hydrostatic thrust gas bearing. This high damping ratio of hydroinertia gas bearings causes high stability in high speed operation.

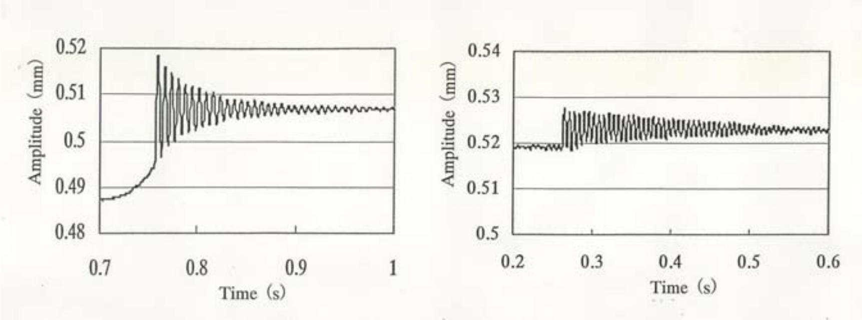

(a) Hydroinertia thrust gas bearing (b) Conventional hydrostatic gas bearing

Figure 3-15: Step Response of Thrust Gas Bearings (*ps*=300kPa(G)).

3.3 Herring-Bone & Spiral-Groove Hydrodynamic Gas Bearings

The journal bearings with Herring-bone grooves and the thrust bearings with spiral grooves are very popular hydrodynamic gas bearings. The methods of design and analysis are explained in many textbooks [4]. The whirl stability limit is also shown in many textbooks, although they are very empirical, and the applicability to the micro bearings is not clear. Figure 3-16 shows the stability limit of the herring-bone journal bearing of the diameter 4mm. Relatively large stable region is seen in the figure, however, the bearing clearance is required to be smaller than 4µm to be in the stable region, which is very difficult to control, both from the fabrication technology, and from the way to absorb the heat expansion. With such a small bearing gap, the heat generated by the shear of the gas in the bearing clearance is expected to be very large. Since the wall of the Herring-bone bearing is a hard wall, and it won't have any compliance, the issue of heat expansion will be very important to be solved to use in micromachine gas turbines. It is also a demerit on passing through the resonance speed. Since the bearing clearance is extremely small and the wall has no compliance, the rotor should be balanced to very high level.

(a) Test Rig **(b) Rotor**

Figure 3-16: Suction Bearing which achieved 1,200,000 rpm.

3.4 Foil Hydrodynamic Gas Bearings

As it is shown in Figure 3-3, there are varieties of foil bearings. The type of the foil bearing that is though to have the largest load capacity with large damping is the bump foil type, which is shown in the center of Figure 3-3. The foils consist of the bump foil and the top foil. The top foil is a smooth foil is a foil facing to the rotor shaft to create wedges to generate dynamic pressure. The top foil will rub the shaft at every start up and stopping operation, and it will define the life of the foil bearings. To prevent the wear and the burning of the foil and the shaft during the rub, special coating is usually applied to the surface of the top foil, of which the contents of the coating material is the top secret of each manufacturer.

The bump foil is located between the top foil and the bearing housing. It defines the geometry of the top foil, and also creates damping by the friction with the top foil and the housing. Sometimes, multiple layers of the bump foils are used. In such a case, the friction between the bump foils will also create large damping. The bump foil is designed to create small waviness to the top foil to trap the gas into the pocket, just as Herring-bone bearings are doing.

In addition to the coating technology and the damping prediction technology, the technologies for foil bearings includes the prediction of the pressure distribution on the top foil, and the technology to fabricate the bump foils to realize the designed pressure distribution. Foil bearing doesn't require the high accuracy for the diameter, but the shape of the bump to catch the air in the center of the bearing will require special fabrication techniques. In micro foil bearings, it is also very difficult to measure the pressure distribution to verify the fabrication accuracy.

3.5 Latest Micro-High-Speed Bearing Technologies in the World

Currently, there are several groups in the world developing man-portable power generators. The most famous and the largest project is the MIT Microengine Project [5]. They are trying to realize 50W class gas turbine generator only by using Microelectromechanical Systems (MEMS) fabrication technologies. This is a revolutionary concept, and the product, if realized, has a large impact on the market of portable electric appliance and power generation. However, since the technology is so different from the current technology for the gas turbines, the project is already taking more than a decade. They have developed a very thin gas bearing to be fabricated by MEMS technology, and ran up to 1,370,000 rpm [6], but it requires more researches for practical use. They may achieve a self-sustained operation of the prototype engine within a couple of years, but the realization of the practical microengine based on MEMS fabrication technology will require another decade.

For more conventional micromachine gas turbine that has three dimensional geometry scaled down from typical modern centrifugal turbomachines in larger scale, Honda has demonstrated a micro turbocharger of impeller diameter 12mm, but they used existing micro-ball bearings in market, and the maximum shaft speed was limited to 450,000 rpm at short time, which is merely 55% of the design speed [7]. Likewise, most of the researchers used ball bearings [8] to prevent being dragged in to the deep meadow of bearing development.

One important development on gas bearing to be noted is the micro-foil bearing developed by Mohawk Innovative Technology Inc. (MiTi). They developed a micro-foil bearing of diameter 6mm, and successfully demonstrated to stably run up to 700,000 rpm [9].

The highest speed achieved by three-dimensional rotor is 1,200,000 rpm at a shaft of diameter 4mm, for Solid Nuclear Magnetic Resonance (NMR) Spectroscopy by using hydroinertia gas bearings [10] (Fig. 3-16). The bearing for the NMR has a very special configuration which the rotor shape is limited to a plain 4mm diameter shaft without load and without any parts of diameter larger than 4mm.

4.0 DESIGN METHDS

4.1 Load Capacity *W* and the Stiffness *k* of the Gas Bearings

There are number of methods to calculate the load capacity of the variety of gas bearings. The load capacity of hydrostatic gas bearings can be calculated by assuming the linear pressure distribution in the bearing clearance that the supply gas pressure at the supply gas hole reduces linearly toward the ambient pressure at the bearing edge. However, recently, more sophisticated three dimensional computational fluid dynamics (CFD) programs are also used to obtain more quantitative and detailed information on the flow in the bearing clearance. Hydrodynamic gas bearing requires sophisticated CFD calculations or detailed test data to calculate the load capacity. The data published by MTI [11] and University of Southampton [12, 13] have long been used for the design bases. Those methods are already explained in many literatures ([4] for example), hence, will not be reviewed, here.

The flow in the bearing clearance of the hydroinertia gas bearing contains shock wave, and therefore, the calculation of its load capacity is expected to require a sophisticated method as three dimensional compressible CFD. However, a relatively simple method to calculate the load capacity without sophisticated three dimensional CFD tool has recently developed [10]. The new method is explained in this section.

Note that the bearing stiffness *k* can be calculated from the change of the load capacity due to the change of the bearing clearance *Cr*, as follows.

$$k = -\frac{dW}{dCr}. \tag{4.1.0}$$

4.1.1 Load Capacity of a Hydroinertia Circular Thrust Bearing

4.1.1.1 Calculation Methods

Fig. 4-1 shows a calculation model of a hydroinertia circular thrust gas bearing. The bearing has a gas supply hole of inherent orifice type at its center. The bearing clearance *h* and the diameter *d* of the gas supply hole are relatively large compared with the bearing radius R_0. The inertia effect of gas flow in the bearing clearance is assumed to be predominant to viscous effect. The flow area of gas in the bearing clearance is the minimum at the imaginary cylindrical surface imagined at the exist of the supply hole shown by a broken lines in Fig. 4-1, and the flow is choked at this point. The coordinate *x* is taken along the bearing radius. The supply pressure of gas is p_s and the ambient pressure is p_a.

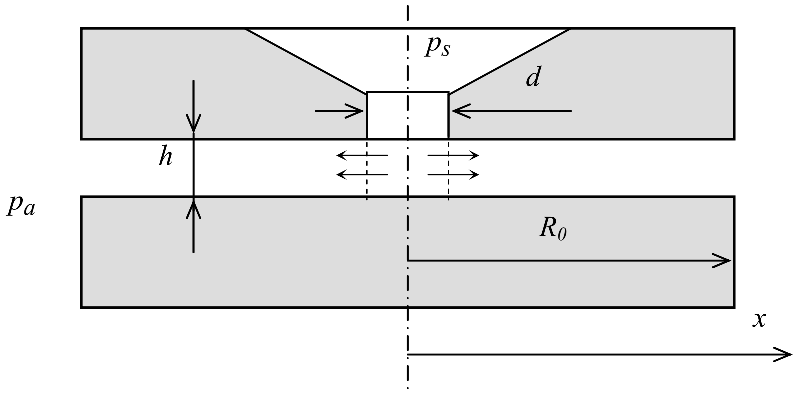

Figure 4-1: Hydroinertia Circular Thrust Gas Bearing.

Supposing a compressible adiabatic flow with wall surface friction and applying its equations for the steady condition to the flow in the bearing clearance, distributions of Mach number and of pressure are given by following equations.

$$\frac{dM}{dx} = \frac{\Lambda}{1-M^2}, \tag{4.1.1}$$

$$\frac{dp}{p} = \frac{\kappa M^2}{1-M^2}\frac{dA}{A} + \frac{\kappa M^2[(\kappa-1)M^2+1]}{2(M^2-1)}\left(\frac{\lambda}{4m}\right)dx, \tag{4.1.2}$$

where, Λ is

$$\Lambda \equiv M\left[1+\frac{\kappa-1}{2}M^2\right]\left[\frac{\kappa M^2}{2}\left(\frac{\lambda}{4m}-\frac{1}{A}\frac{dA}{dx}\right)\right], \tag{4.1.3}$$

and κ is adiabatic index, A is flow area at Mach number M, and m is hydraulic mean depth and is given by $m=h/2$.

λ is the coefficient of wall surface friction and is given by following equations depending on Mach number[3.1)]. For $M<1$, the gas flow in the bearing clearance is assumed to be laminar, and λ is given by,

$$\lambda = 96\mu / 2h\rho u = 96 / Re. \tag{4.1.4}$$

For $M \geqq 1$, the flow is assumed to be turbulent, and λ is calculated from following equation,

$$Re = \sqrt{8/\lambda}\, e^{0.41\left(\sqrt{8/\lambda}-2.4\right)}, \tag{4.1.5}$$

where Re is Reynolds number defined by following equation using $2h$ as representative length, u as flow speed and ν as dynamic viscosity.

$$Re=2hu/\nu \tag{4.1.6}$$

The relation of Mach numbers M_1, M_2 and pressures p_1, p_2 ahead of and behind the shock are given by following equations.

$$M_2{}^2 = \frac{(\kappa-1)M_1{}^2+2}{2\kappa M_1{}^2-(\kappa-1)} \tag{4.1.7}$$

$$\frac{p_2}{p_1} = \frac{2\kappa M_1{}^2-(\kappa-1)}{\kappa+1} \tag{4.1.8}$$

As the flow is choked at the cylindrical surface imagined at the exit of the supply hole, flow rate $\dot{m}$ of the bearing gas is give by

$$\dot{m} = \frac{p_s Ac}{\sqrt{RTs}} M\sqrt{\kappa}\left(1+\frac{\kappa-1}{2}M^2\right)^{-\frac{\kappa+1}{2(\kappa-1)}}, \tag{4.1.9}$$

where, p_s is the supply gas pressure, Ts is the supply gas temperature, c is the flow coefficient of inherent orifice and R is the gas constant.

Mach number at the exit of the bearing is given by

$$(\kappa-1)M_e{}^4 + 2M_e{}^2 - \frac{2\dot{m}^2 RT_s}{\kappa A_e{}^2 p_a{}^2} = 0, \tag{4.1.10}$$

where, A_e is the flow area at the exit of the bearing and p_a is the ambient pressure.

Using these equations, the distribution of the Mach number and the pressure along the bearing clearance can be calculated in following steps by PCs.

(1) Starting from the Mach number at the bearing exit that is given by equation (4.1.10), Mach number distribution downstream of the shock wave is numerically calculated upward by equation (4.1.1) using Renge-Kutta method.

(2) At the presumed location of the shock wave, upstream Mach number M_1 is calculated by equation (4.1.7).

(3) Then the calculation of equation (4.1.1) is continued up to the imaginary cylindrical surface at the exit of the gas supply hole.

(4) This procedure is repeated until the shock wave position that makes the Mach number at the exit of supply hole to unity is found.

(5) Once the distribution of Mach number is obtained, the pressure distribution in the bearing clearance is calculated by equation (4.1.2).

Load capacity W is obtained by integrating the gauge pressure over the bearing surface. Force generated by the impact of gas flow from the supply hole against the bearing wall should be added to the load capacity. This force F is given by following equation.

$$F=M\,(\kappa RT)^{1/2} \tag{4.1.11}$$

4.1.1.2 Validation Test

Experiment has been conducted to validate the calculation tool. Fig. 4-2 shows the test rig to measure the static characteristics of hydroinertia circular thrust gas bearings. The upper stage of the circular thrust bearing with a supply hole at the center is set on the xyz-stage of a three-dimensional coordinate measurement machine (CMM). The diameter of the circular thrust bearing and the supply hole are 10mm and 1mm, respectively. The Z-axis is adjusted to obtain a desirable bearing clearance, then the X and the Y axis are traversed to scan the bearing surface to measure the pressure distribution. The pressure in the bearing clearance is measured by a semiconductor type pressure probe ((9) in Fig. 4-2) through a 0.3mm diameter pressure port((8) in Fig. 4-2). The load capacity is measured by the electronic balance ((6) in Fig. 4-2). To compensate the vertical displacement of the electronic balance due to the change in bearing load, the vertical displacement of the thrust plate is measured by an electric micrometer.

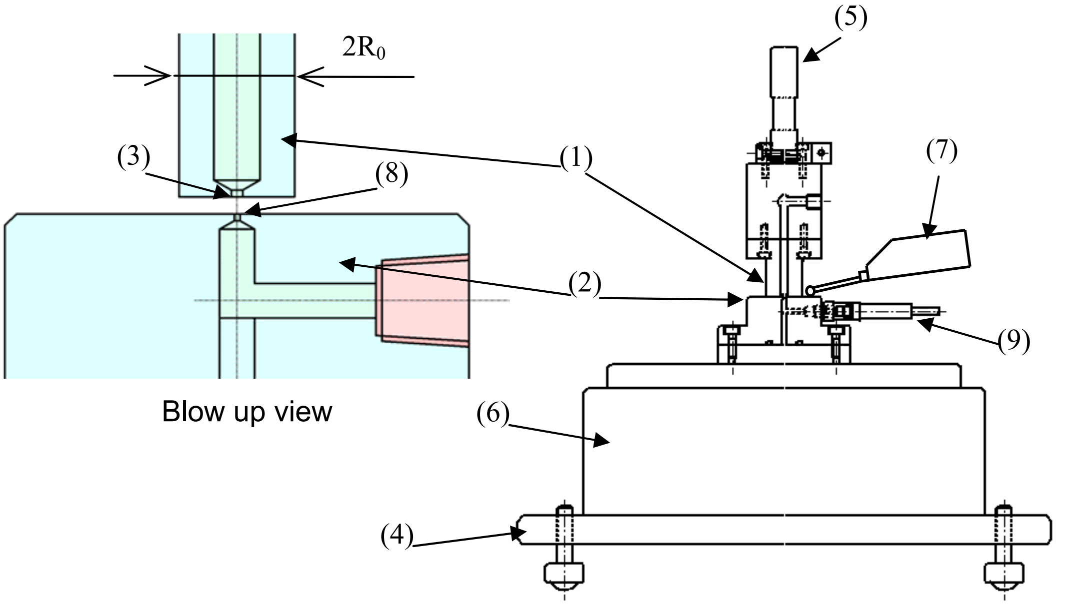

(1) Circular thrust bearing; (2) Thrust plate; (3) Air supply hole; (4) Adjustable table; (5) Bearing holder; (6) Electronic balance; (7) Micrometer; (8) Pressure port; (9) Pressure probe.

Figure 4-2: Test Rig for the Hydroinertia Circular Thrust Gas Bearing.

Fig. 4-3 shows the pressure distribution of a hydroinertia circular thrust gas bearing. In these cases, the bearing clearances are large enough to choke the gas flow at the exit of the supply hole and the negative gauge pressure (pressure less than the ambient pressure 100kPa) is seen in the supersonic flow region near the exit of the supply hole. The calculation result showed a good match to the experiment, with small mismatch of the shock position.

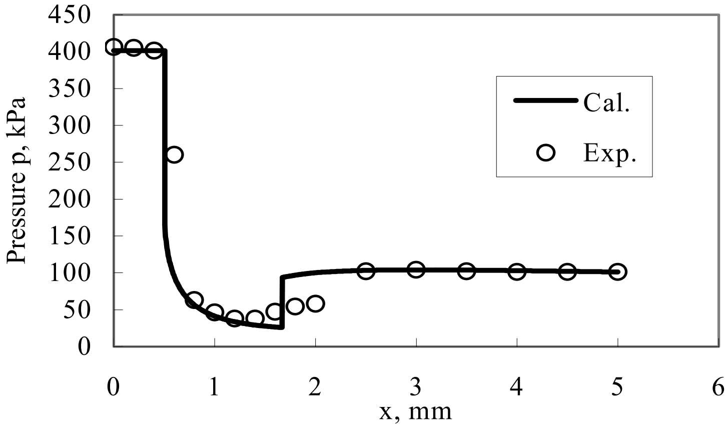

Figure 4-3: Pressure Distribution of a Hydroinertia Circular Thrust Gas Bearing
R0=5mm, d=1mm, h=0. 2mm, ps=300kPa(gauge).

Fig. 4-4 shows the pressure distribution for the case of small bearing clearance. In this case, the flow is not choked at the exit of the supply hole and negative pressure and shock wave are not observed. The calculated values in this figure are obtained by the same equations with the case of large bearing clearance. As shown in the figure, calculated values agree well with the experimental values, and the calculation method developed in the previous section has been validated for predicting the steady pressure distribution in the hydroinertia circular thrust bearings with various bearing clearance.

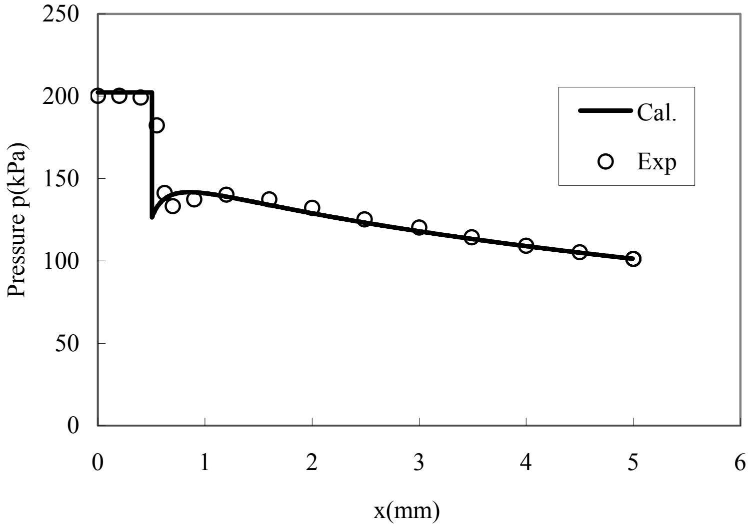

***R_0*=5mm, *d*=1mm, *h*=0. 030mm, *p_s*=100kPa(gauge)**

Figure 4-4: Pressure Distribution of a Hydrostatic Circular Thrust Gas Bearing.

Fig. 4-5 shows the load capacity and flow rate of the hydroinertia circular thrust gas bearings The load capacity decreases with increase in bearing clearance and it becomes negative, that means load capacity is generated by suction force. As shown in Fig. 4-5, load is supported by suction force when the bearing clearance exceeds about $h \fallingdotseq 0.07$mm for the small bearing, and $h \fallingdotseq 0.13$mm for the large bearing. In the region of large bearing clearance, as the load capacity by suction force becomes almost constant and the bearing stiffness becomes almost 0. The calculation matched well to the measurement. Hence the calculation program has successfully been validated as a tool to simulate the aerodynamics in hydroinertia circular thrust gas bearings.

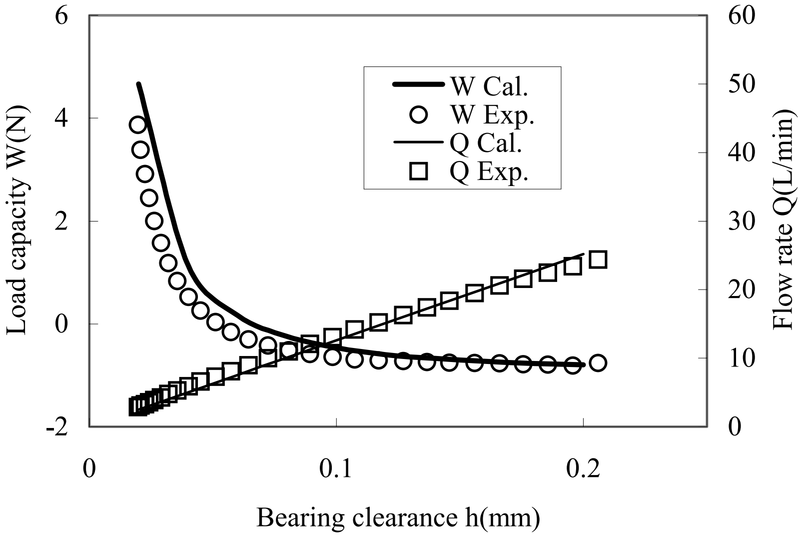

Figure 4-5: Load Capacity and Flow Rate of a Hydroinertia Circular Thrust Bearing
***R_0*=5mm, *d*=1mm, *p_s*=300kPa(gauge).**

4.1.2 Load Capacity of a Hydroinertia Journal Bearings

4.1.2.1 The Calculation Methods

A single admission inherent orifice type radial bearing shown in Fig. 4-6 is chosen as an analytical model of hydroinertia radial gas bearings. Its radial clearance C_r and the diameter of the supply holes d are relatively large compared with those of usual hydrostatic gas bearings.

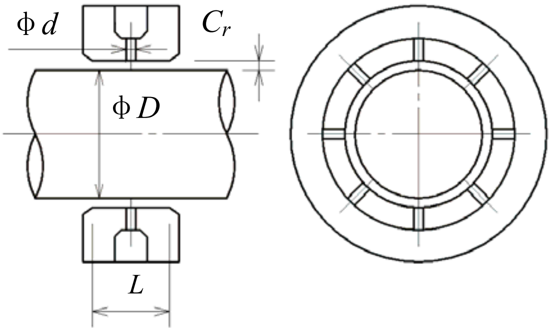

Figure 4-6: Single Admission Hydroinertia Radial Gas Bearing.

In hydroinertia gas radial bearings, it is difficult to determine the position of the shock wave in the flow from each supply hole by simple calculations. A radial bearing is approximated by replacing each of the supply hole by a hypothetical circular thrust bearing as shown in Fig. 4-7.

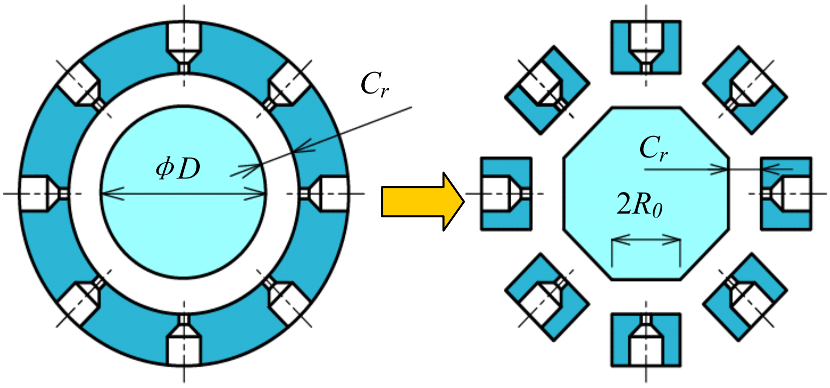

Figure 4-7: Model for the Hydroinertia Journal Gas Bearing.

Fig. 4-8 shows the relation between a developed surface of the radial bearing covered by one supply hole and a hypothetical circular thrust bearing. In the radial bearing, gas from a supply hole flows in radial direction up to the radius x_t of which the circumferential length equals to the outlet width of the radial bearing, and then flows uniformly in constant cross sectional area. The radius R_0 of the hypothetical circular thrust bearing is taken as the mean value of the vertual streamline length l_i supposed in the radial bearing and is calculated by the following equations.

$$R_0 = \frac{1}{n_k + 1} \sum_{i=1}^{n_k+1} l_i \qquad (4.1.13)$$

$$l_i = \frac{L_b - \Delta L_a \cdot (i-1)}{\cos(\Delta\theta \cdot (i-1))} \{(1 - \sin(\Delta\theta \cdot (i-1))\} + L_b \qquad (4.1.14)$$

where, $L_a = \pi D/2n$, $L_b = L/2$, D is the bearing diameter, L is the bearing length, n is the number of supply holes, n_k is the number of the flow segments taken in the bearing clearance and $\triangle\theta = \pi/n$.

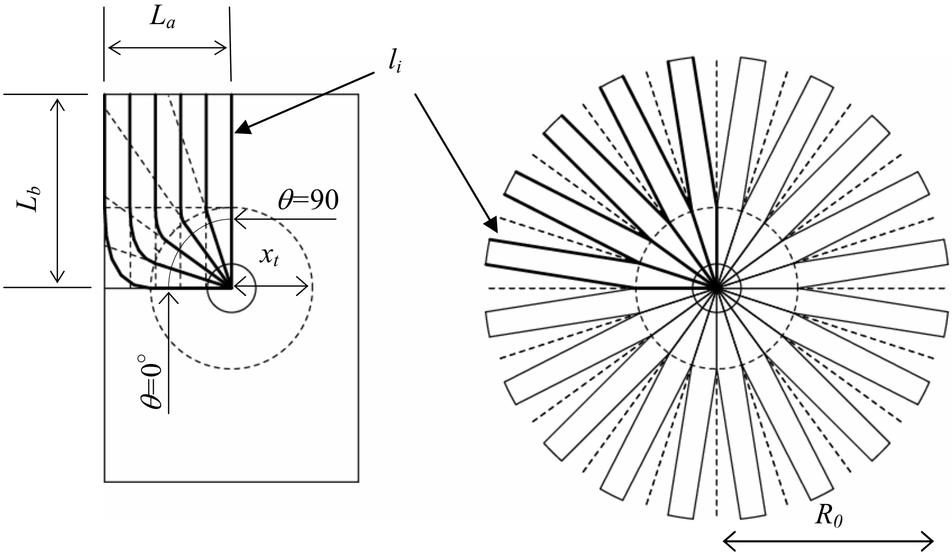

Figure 4-8: Developed Surface of the Radial Bearing and a Hypothetical Circular Thrust Bearing.

Radius x_i should be corrected by expansion factor c_b because of the effect of flow inflection and expansion from a point source. Then the radius x_i is given by $x_i = c_b \cdot D/n$. The expansion factor c_b is taken as $c_b = 0.8^{4)}$.

In the case that the shaft is located at an eccentric position to the bearing, the clearance h of each hypothetic circular thrust bearing is given by following equation.

$$h = C_r(1 - \varepsilon\cos\theta) \qquad (4.1.15)$$

where, C_r is the radial clearance, ε is the eccentricity ratio defined by e/C_r, e is the eccentricity, and θ is the angle between the direction of eccentricity and the normal to the surface of the hypothetical circular thrust bearings.

Fig. 4-9 shows an example of load capacity and flow rate of a hydroinertia radial gas bearing. The bearing diameter D=4mm, length L=2.4mm, diameter d of the supply holes d=0.3mm and number n of the supply holes n=8 and supply pressure p_s=150kPa(G). Load capacity becomes maximum at C_r=28μm for ε=0.3 and C_r=35μm for ε=0.5.

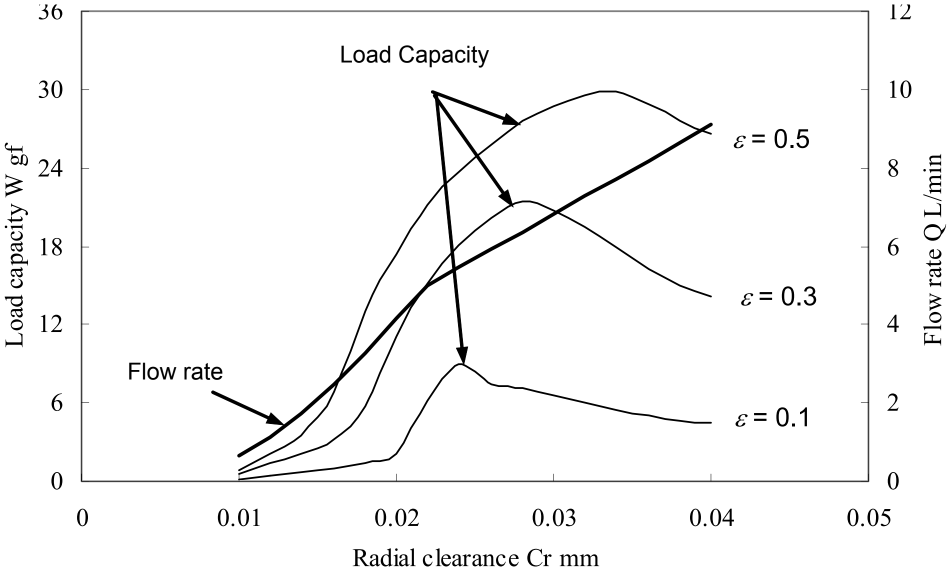

Figure 4-9: Load Capacity and Flow Rate of a Hydroinertia Radial Gas Bearing.

In hydroinertia radial gas bearings, if the rotor displaces from the center position, suction force is generated in the large clearance side and repulsive force is generated in the small clearance side. Therefore, the load capacity, that is the sum of the repulsive force and the suction force, is always positive, and the restoring force to the rotor eccentricity is much bigger than that of the conventional hydrostatic radial gas bearings.

4.1.2.2 Validation of the Method

Fig. 4-10(a),(b) show the relation between the radial clearance and flow rate of two different configurations of hydroinertia radial gas bearings. The dimensions of the radial bearings are listed in Table 4-1. Bearing1 is the radial bearings for solid NMR spinners and Bearing2 is for that the micro turbo chargers.

Table 4-1: Dimension of the Hydroinertia Radial Gas Bearings

	Bearing 1	Bearing 2
Diameter *D*	4 mm	4 mm
Length *L*	2.4 mm	4 mm
Diameter of supply hole *d*	0.35 mm	0.3 mm
Number of supply holes *n*	8	8

In Fig. 4-10, the solid lines are calculated values and the circles are the measured values. Radial clearance of the bearings is adjusted by inserting various diameters of with pin gauges into the bearings. As shown in the figures, measured values well agree with calculated values.

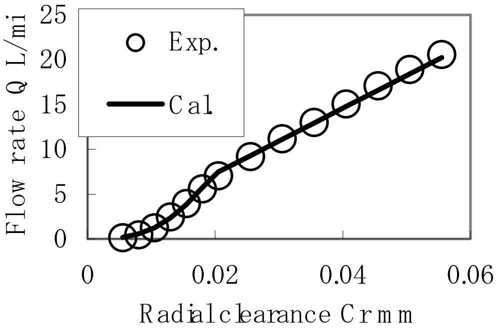

(a) Bearing 1; L/D=0.6, p_s=300kPa(G)

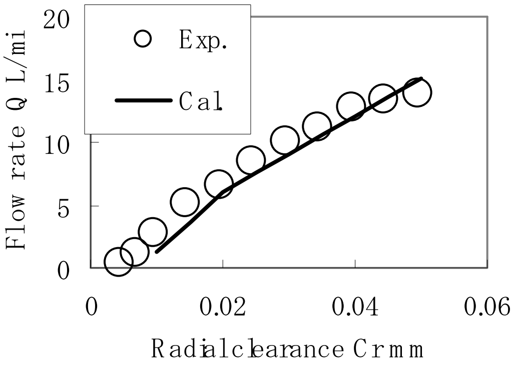

(b) Bearing 2; L/D=1, p_s=300kPa(G)

Figure 4-10: Flow Rates of the Hydroinertia Radial Gas Bearing.

In small radial clearance region, that is less than 20μm in the figure, flow in the bearing clearance is governed by viscosity, so the flow rate increases in proportion with the third power of the radial clearance. In large radial clearance region, flow rate increases in proportion with the radial clearance. This means the flow is choked at the exit of the supply holes.

Fig. 4-11(a),(b) show the calculated relation between the eccentricity *e* and the load capacity *W*. Fig. 4-11(a) is the case of Bearing1 with radial clearance C_r of 31 μm and (b) is the case of Bearing2 with radial clearance C_r of 30 μm. Eccentricity e is calculated from the eccentricity ratio ε by following equation e= ε Cr. As shown in the figures, the load capacity is proportional to the eccentricity in small eccentricity region. The bearing stiffness k can be calculated from the slope of the load capacity against the eccentricity in Fig. 4-11 as follows: k1=22.57kN/m (Bearing1, ps=150kPa), k2=34.75kN/m (Bearing1, ps=300kPa) and k3=71kN/m (Bearing2, ps=300kPa).

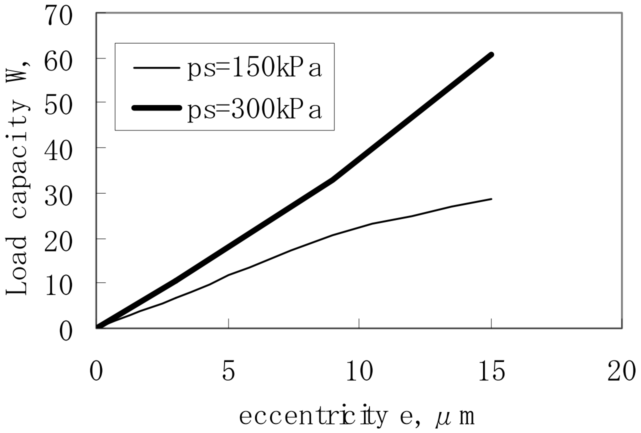

(a) Bearing1 C_r=31 μm

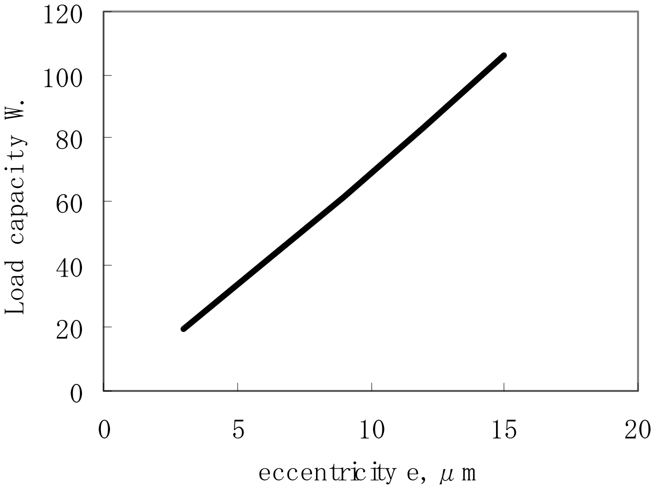

(b) Bearing2 C_r=30 μm

Figure 4-11: Load Capacity of Hydroinertia Radial Bearings.

Resonance frequency N_1 for the cylindrical mode is given by

$$N_1=(k/m_w)^{1/2}/2\pi \tag{4.1.16}$$

where, m_w is half of the mass of the rotor per bearing.

Substituting the bearing stiffness and the mass of the spinners to equation (4.1.16), resonance frequency are calculated as follows: N_l=1033Hz (Bearing1, p_s=150kPa), N_l=1281Hz (Bearing1, p_s=300kPa) and N_l=650Hz (bearing2, p_s=300kPa).

Fig. 4-12 shows the spectrum of the spinner vibration near the resonance frequency. These vibration spectrums are obtained without spinner rotation. In general, inherent orifice type restrictors have high stability to pneumatic hummer instability. However, with large bearing clearance such as hydroinertia gas bearings, impact force of the supply gas may cause excitation force to the shaft and the small rotor vibration may occur at the resonance frequency. Hence, it is important to predict the shaft vibration accurately to avoid resonance. In the micro spinner, the amplitude of the vibration is extremely small (under 0.5μm), and there is no problem for bearing performance.

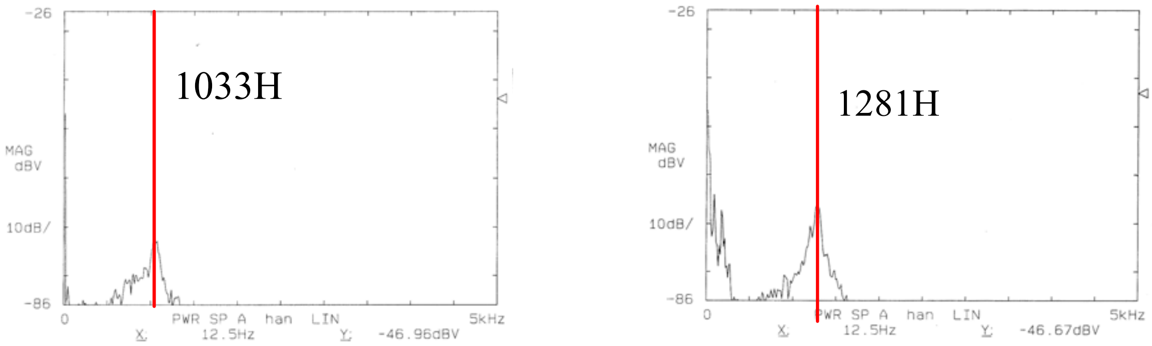

(a) Bearing1, p_s=150kPa(G) **(b) Bearing1, p_s=300kPa(G)**

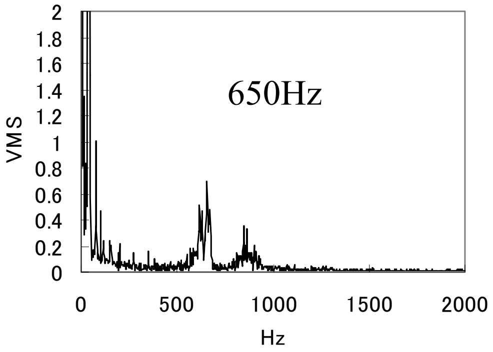

(C) Bearing2, p_s=300kPa(G)

Figure 4-12: Vibration Spectrum near first Resonance Frequency.

As shown in the figures, calculated resonance frequency agrees well to that of measured value. This proves that the calculation method explained in previous section is appropriate to predict the performance of hydroinertia radial gas bearings.

The final validation of the calculation method has been conducted by a segment test of a radial bearing. Figure 4-13 shows the test rig for measuring the static characteristics of a segment of hydroinertia radial gas bearing corresponding to the left figure of Figure 4-8. Construction of the test rig and measuring method are almost the same as the test rig for hydroinertia circular thrust gas bearing shown in Fig. 4-2, but the shape of the bearing surface to be tested is rectangle with side boundary being restricted by the edge of two plane bearings on the side surface to simulate the flow pass in the radial bearing. The pressure distribution in the bearing clearance, the load capacity and the flow rate are measured in the test rig. Dimension of the test plane bearing is as follows: bearing length L_b=20mm, diameter of the supply hole d=2mm. Bearing clearance, that corresponds to the radial clearance, is adjusted by clearance adjusting block and Z position of XYZ stage.

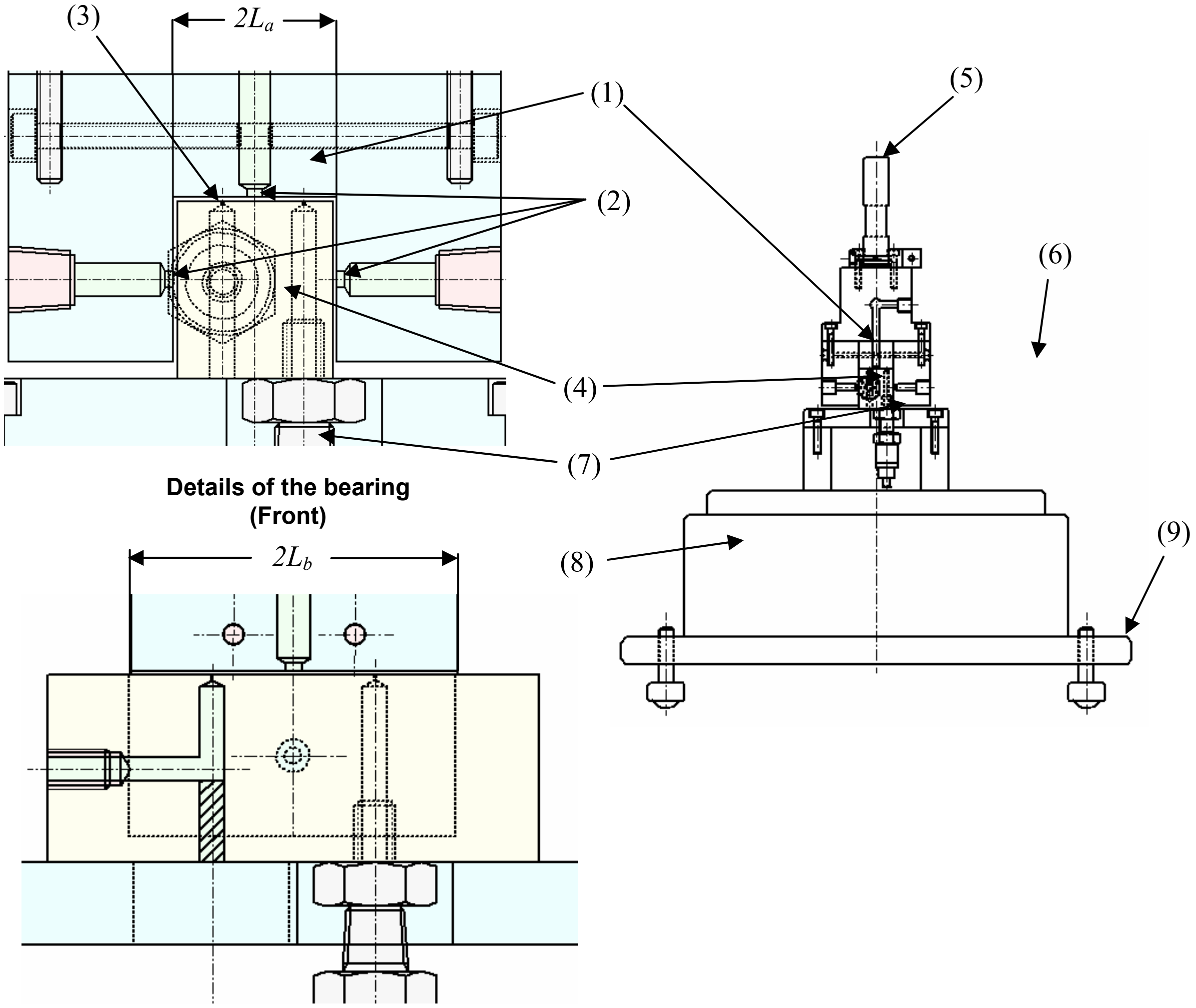

Details of the bearing
(Front)

Details of the bearing
(Side)

(1) Plane radial bearing (test bearing); (2) Air supply hole; (3) Pressure port; (4) Clearance adjust block; (5) Bearing holder; (6) Micrometer; (7) Pressure probe; (8) Electronic balance; (9) Adjustable table.

Figure 4-13: Test Rig for the Hydroinertia Radial Gas Bearing.

Fig. 4-14 shows the pressure distribution. The diameter of the pressure ports is 0.2mm and they are positioned at 2mm, 4mm, 6mm, 8mm from the bearing center line. The test plane bearing scans in Y direction and measures the pressure in the bearing clearance.

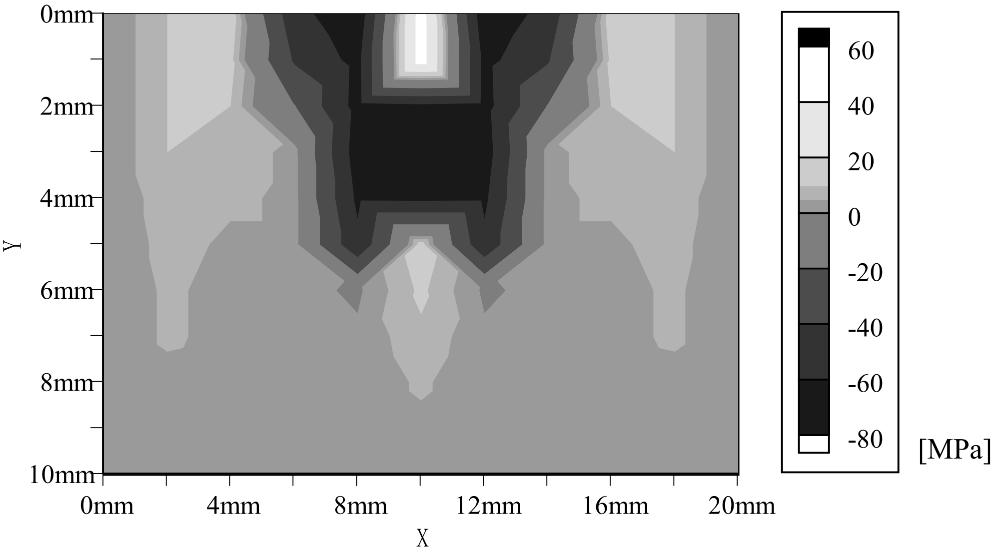

Figure 4-14: Pressure Distribution of a Hydroinertia Radial Gas Bearing.

Figure 4-15 shows the load capacity *W* and the flow rate *Q*. As shown in the figure, calculated values agree well with the measured values, and the method has been validated as the design tool to calculate the load capacity of radial bearings.

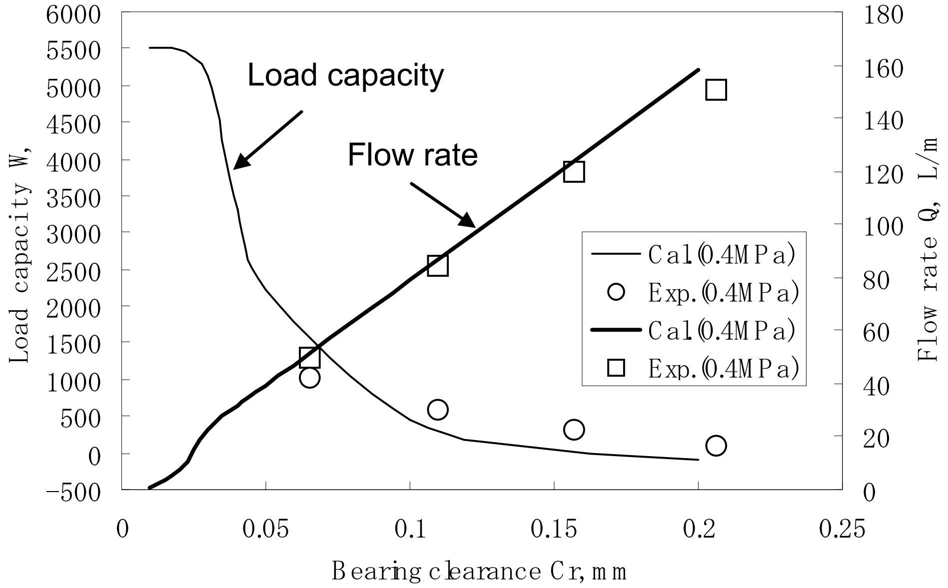

Figure 4-15: Load Capacity and Flow Rate of a Hydroinertia Radial Gas Bearing.

4.2 Bearing Loss

Viscous loss of the gas bearing is proportional to square of the rotor speed and the bearing clearance. Therefore, at the high rotational speed, large difference in the bearing loss appears between different bearing configurations, such as hydro-inertia gas bearing and dynamic gas bearings. Viscous loss of the gas bearings at variety of bearing clearances and shaft speeds are shown in Figure 4-16. At current scale, the total viscous loss of two thrust bearings and two radial bearings is 12W by hydroinertia gas bearings, and is 68W by dynamic gas bearings that the bearing clearance is as small as 5µm. Hydroinertia gas bearings consumes 56W less power than the hydrodynamic gas bearings per rotor.

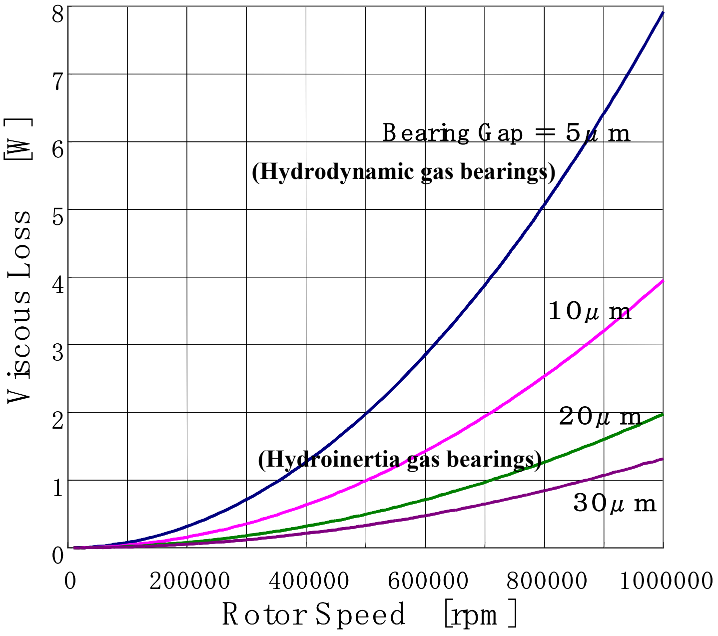

(a) Journal bearings (L=D=4mm)

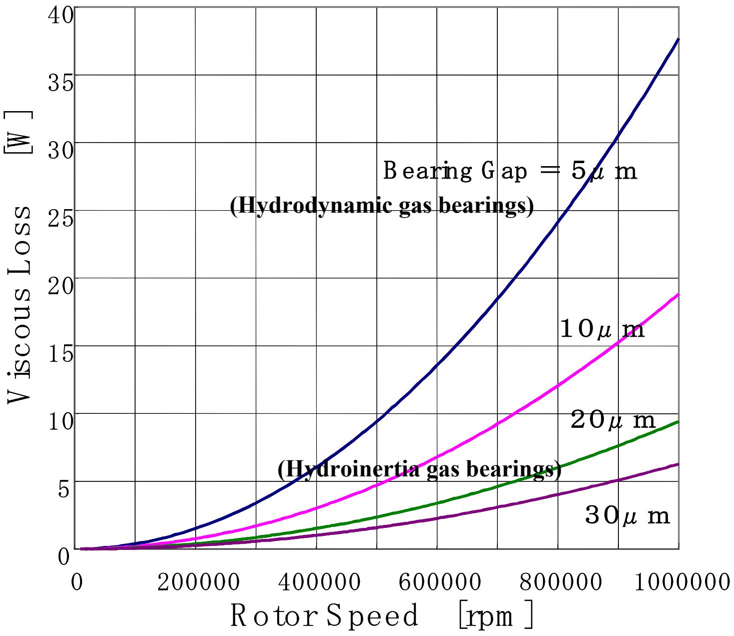

(b) Thrust bearings (D_{out}=10mm, D_{in}=5mm)

Figure 4-16: Viscous Loss of Gas Bearings.

The drawback of the hydroinertia gas bearing is the relatively large amount of the supply gas required for the operation. For current target micromachine gas turbine system, hydroinertia gas bearings are expected to consume about 20 liter/minute of compressed air from the compressor exit, which corresponds to approximately 20% of the compressor air. This corresponds to about 50W when the compressor efficiency is 80%. Hence it should be noted that the advantage of the low viscous loss can be set off by the power required to generate the supply air, if the supply air generator is included in the system. If the compressor efficiency is lower, the power required to generate the bearing supply gas increases, and hydrodynamic gas bearings may have advantage.

Although much advantage may not be expected from the power account, the large advantage of the hydroinertia gas bearings lies in the large loading capacity, large stability against the whirl at extra-high speed, and in the relatively low requirement for fabrication accuracy that is difficult to achieve at machining at micro scale.

The bearing loss of the ball bearings can be estimated from the friction coefficient μ that is shown in the catalog of bearings. The power loss can be calculated as a product of the friction coefficient, the load, and the peripheral speed. Ball bearings usually need to be pre-loaded to confirm the contact of the ball to prevent skidding. The magnitude of the pre-load will be decided from the unbalance level to allow. If the shaft has an unbalance of mr per bearing, where m is the mass of the shaft per bearing and r is the displacement of the center due to the unbalance, the centrifugal force due to the unbalance is $mr\omega^2$, where ω is the angular rotating speed. For a shaft of 1g-μm of unbalance rotating at 870,000 rpm, the maximum loading will be 8.3N.Hence, this amount of pre-loading is required to prevent skidding, and the average load due to the unbalance and the pre-loading becomes 12.5N. Then the power loss for 4mm bearings will be 34W per a bearing, and 68W per rotor, assuming two bearings per rotor. This looks compatible loss to that of the gas bearings. However, there are two loss components not included in this analysis. Those are the viscous loss by lubrication oil, and the power for the oil pump. The viscous loss will become relatively large at micro-scale, and will be larger than the viscous loss of the gas bearings. The power for the oil pump can be large, but it depends on the design. In any case, the total loss of the ball bearing is expected to be more than twice the loss of gas bearings.

4.3 Whirl Instability Limit

The operation range of the gas bearings at high speed is known to be limited by an instability called whirl. The cause of the whirl is the interaction of the motion of the shaft and the hydrodynamic force inside the radial bearing clearance that generates tangential force to excite the whirling motion of the shaft. By the classical analysis of the bearing flow based on the Reynolds equation that assume incompressibility for the bearing flow, the whirl force occurs at half the rotational frequency [14], and when the whirl frequency meets the resonance speed of the rotor, the whirl oscillation diverge, and the bearing fails by the rotor hitting the bearing. This suggests that the rotor cannot run up to the speed higher than twice the resonance speed. Since the hydrodynamic effect is small at low speed, the first resonance speed may sometimes be passed through. However, there always exists higher order resonance speed that limit the maximum achievable shaft speed by whirl instability.

The analysis of whirl instability can be done by solving the dynamic equation of the rotor motion by assuming an oscillatory solution in a form of $e^{j\omega t}$, and find the condition to make the amplitude of the oscillatory motion to increase in time. The basic equation of the rotor motion can be written as follows.

$$m\frac{d^2e}{dt^2}+C\frac{de}{dt}+ke=0, \qquad (4.3.1)$$

where, e is the eccentricity of the rotor, m is the rotor mass per bearing, C is the system damping, and k is the hydrodynamic stiffness. The stiffness k consists of hydrostatic stiffness k_s and hydrodynamic stiffness k_d working in orthogonal direction each other, and the hydrodynamic stiffness consists of that due to pumping effect k_p and that due to viscous effect k_v as follows.

$$k = k_s - jk_d = k_s - j(k_p - k_v)\,. \qquad (4.3.2)$$

The remaining issues are the modelling of the stiffness *k* and the damping *C*. The analysis by Spakovszky et al. [15, 16] showed a possibility of increasing the whirl ratio by a model including the inertia effect and assuming small *L/D*. The whirl ratio ω/Ω, which is the rotational frequency divided by the whirl frequency, has been calculated as follows.

$$\frac{\omega}{\Omega} = \frac{2}{1 - \dfrac{\left(C_r / R \right)}{2\left(L / D \right)^2}} \qquad (4.3.3)$$

The whirl ratio can be increased by changing the aspect ratio *L/D* and the bearing clearance *Cr*. The analysed results of the *L/D* effect is shown in Figure 4-17. The results showed good match with the test result of MIT type static gas bearings with very small *L/D*, but it did not match to the test results of hydroinertia gas bearing with *L/D* equals to 1. The whirl ratio is about 2 in analysis over all the range of bearing clearance, but the test result was 9. The analysis by Spakovszky includes the inertia effect of the bearing gas, but does not include the compressibility effect. Also, the circumferential pressure variation is omitted based on the small *L/D* assumption.

The analyses without these restrictions were performed by Mori et al. [17, 18]. Instead of modeling each terms in dynamic equation (4.3.1), they showed the effect of number of parameters to control the whirl ratio by more detailed analysis based on the modified Reynolds equations with compressibility in the continuity equation. The basic equations are,

x-momentum $$\frac{\rho}{h}\int_0^h \{\frac{\partial u}{\partial t} + u\frac{\partial u}{\partial x} + v\frac{\partial u}{\partial y} + w\frac{\partial u}{\partial z}\}dy + \frac{\partial p}{\partial x} = \mu\frac{\partial^2 u}{\partial y^2}\,, \qquad (4.3.4)$$

y-momentum $$\frac{\partial p}{\partial y} = 0\,, \qquad (4.3.5)$$

z-momentum $$\frac{\rho}{h}\int_0^h \{\frac{\partial w}{\partial t} + u\frac{\partial w}{\partial x} + v\frac{\partial w}{\partial y} + w\frac{\partial w}{\partial z}\}dy + \frac{\partial p}{\partial z} = \mu\frac{\partial^2 w}{\partial y^2}\,, \qquad (4.3.6)$$

continuity $$\frac{\partial \rho}{\partial t} + \frac{\partial(\rho u)}{\partial x} + \frac{\partial(\rho v)}{\partial y} + \frac{\partial(\rho w)}{\partial z} = 0\,, \qquad (4.3.7)$$

where, x, y, z coordinates are in circumferential, axial, and radially inward direction, respectively, with the origin fixed to the center of the supply gas hole. The boundary conditions to solve these equations are,

at $y = 0$: $u = v = w = 0\,,$ (4.3.8)

at $y = h$: $u = U\,,$ (4.3.9)

$$v = U\frac{\partial h}{\partial x} + \frac{\partial h}{\partial t}\,, \qquad (4.3.10)$$

$w = 0$, and (4.3.11)

from the continuity of the mass flow rate at the feeding hole,

$$\dot{m}_{in} = \dot{m}_{out}, \tag{4.3.12}$$

where,

$$\dot{m}_{in} = \frac{C_D \pi d_s n}{2\pi R} \frac{p_s}{\sqrt{\Re T_s}} h\phi, \tag{4.3.13}$$

$$\dot{m}_{out} = 2\frac{p_{z=0}}{\Re T} \Psi \int_0^h w_{z=0} dy. \tag{4.3.14}$$

ϕ is a dimensionless speed of the supply gas, defined as,

$$\phi = \sqrt{\frac{2\kappa}{\kappa - 1} \left\{ \left(\frac{p_{z=0}}{p_s}\right)^{\frac{2}{\kappa}} - \left(\frac{p_{z=0}}{p_s}\right)^{\frac{\kappa+1}{\kappa}} \right\}} \quad \text{for} \quad \frac{p_{z=0}}{p_s} > \left(\frac{2}{\kappa+1}\right)^{\frac{\kappa}{\kappa-1}}, \text{ or} \tag{4.3.15}$$

$$\phi = \sqrt{\frac{2\kappa}{\kappa + 1} \left(\frac{2}{\kappa+1}\right)^{\frac{2}{\kappa-1}}} \quad \text{for} \quad \frac{p_{z=0}}{p_s} \le \left(\frac{2}{\kappa+1}\right)^{\frac{\kappa}{\kappa-1}}. \tag{4.3.16}$$

Substituting (4.3.13), (4.3.14) into (4.3.12), and defining the designing parameter Γ as,

$$\Gamma = \frac{12\mu\alpha R\sqrt{\Re T}}{p_a C_r^2}, \tag{4.3.17}$$

where α is a supply parameter defined by

$$\alpha = \frac{C_D}{\Psi} \frac{d_s n}{4R} \tag{4.3.18}$$

and C_D and Ψ are the discharge coefficient of the inherent orifice and the correction factor for dispersion effect of the discrete feed, the boundary condition of the continuity of the mass flow rate at the feeding hole is written as,

$$\Gamma P_S \phi = -\left(\frac{h}{C_r}\right)^2 P_{\frac{Z}{R}=0} G_{\frac{Z}{R}=0}, \tag{4.3.20}$$

where,

dimensionless effective pressure gradient in z direction;

$$G = \frac{R}{p_a} \left(\frac{\rho}{h} \int_0^h \left\{ \frac{\partial w}{\partial t} + u\frac{\partial w}{\partial x} + v\frac{\partial w}{\partial y} + w\frac{\partial w}{\partial z} \right\} dy + \frac{\partial p}{\partial z} \right). \tag{4.3.21}$$

In case of discrete gas feed holes, the inertia effect of the supplied gas will be somewhat weakened and the feed gas injected radially inward turns into tangential direction at the volumetric flow of ΔQ. This effect can be added by following equations.

$$F_{\frac{Z}{R}=0} = \xi \frac{\Lambda}{H^2}, \tag{4.3.22}$$

where, ω is the rotating speed and,

dimensionless effective pressure gradient in x direction;

$$F \equiv \frac{R}{p_a}\left(\frac{\rho}{h}\int_0^h \{\frac{\partial u}{\partial t} + u\frac{\partial u}{\partial x} + v\frac{\partial u}{\partial y} + w\frac{\partial u}{\partial z}\}dy + \frac{\partial p}{\partial x}\right), \tag{4.3.23}$$

dimensionless local clearance; $H \equiv \dfrac{h}{C_r}$, (4.3.24)

compressibility number; $\Lambda = \dfrac{6\mu\omega}{p_a}\left(\dfrac{R}{C_r}\right)^2$, (4.3.25)

correction factor for the boundary condition of *F*; $\xi \equiv 1 - \dfrac{\Delta Q}{\left(hU/2\right)}$. (4.3.26)

Assuming the isothermal flow, these equations are rewrote into the equations for the pressure *P* and the effective pressure gradient *F* and *G* in x and z direction, respectively. Then linearizing the whirl motion and these three variables by the first order harmonics as,

$$H = 1 + \varepsilon\cos\theta, \tag{4.3.27}$$

$$P \equiv \frac{p}{p_a} = P_0 + P_1\varepsilon\cos\theta + P_2\varepsilon\sin\theta, \tag{4.3.28}$$

$$F = F_0 + F_1\varepsilon\cos\theta + F_2\varepsilon\sin\theta, \tag{4.3.29}$$

$$G = G_0 + G_1\varepsilon\cos\theta + G_2\varepsilon\sin\theta, \tag{4.3.30}$$

where,$\varepsilon=e/Cr$, *e* is the whirl amplitude, *Cr* is the bearing clearance, and θ is the circumferential angle, the basic equations can be solved by numerically integrating under the boundary conditions to obtain P_1 and P_2. The force working on the rotor is then, written as follows.

Radial force: $$W_r = -2\pi R^2 P_a \varepsilon \int_0^{L/D} P_1 d\frac{z}{R}, \tag{4.3.31}$$

Circumferential force: $$W_t = -2\pi R^2 P_a \varepsilon \int_0^{L/D} P_2 d\frac{z}{R}. \tag{4.3.32}$$

At the limit of whirl instability, the circumferential force *Wt* becomes zero, and the rotor starts to whirl at the whirl amplitude *e*. At this time, instead of solving the dynamic equation of the shaft motion, the whirl frequency Ω can be found from the rotational speed to generate the centrifugal force to balance with the radial force *Wr* as,

$$\Omega^2 = -\frac{2\pi R^2 P_a}{mC_r}\int_0^L P_1 dz\,, \tag{4.3.33}$$

where m is the mass of the rotor per journal bearing.

The results of the calculations are shown in Figure 4-18 (a) and (b). The calculation result contains an unknown parameter ξ, which has to be found by matching to the test results. In current radial bearing, the design parameter Γ defined by (4.3.15) is found to be

$\Gamma = 0.43$,

where

α = supply parameter defined by (4.3.18) = 0.32,

C_D = discharge coefficient of the inherent orifice = 0.85, and

Ψ = coefficient factor for dispersion effect of discrete feed = 0.8.

Therefore, from Figure 4-18 (b), the solution to match the test data is found to exist at about

$\xi = 0.7$.

Then the selection of the parameters to realize the required whirl ratio for the stable operation at 870,000 rpm will be found from the parametric calculation. The whirl ratio can be increased by reducing the *L/D*, increasing the diameter or the number of the bearing gas supply holes. The penalty for these treatments is the reduction of the stiffness and the load capacity. The reduction of the stiffness will cause the reduction of the resonance speed. Since the maximum achievable speed is the product of the resonance speed and the whirl ratio, the optimum parameters should carefully be selected after experimentally verifying the change of whirl ratio, to achieve the increase of the maximum achievable speed.

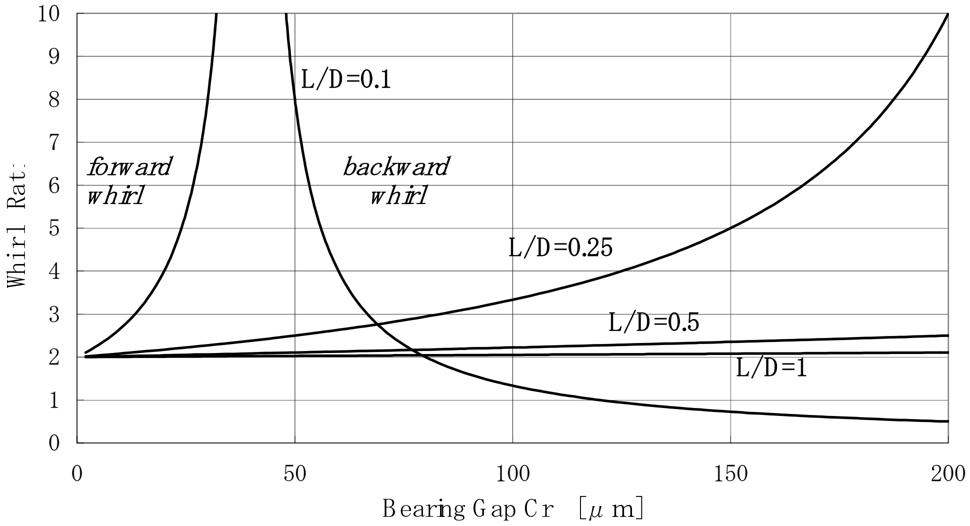

Figure 4-17: Effect of L/D on the Whirl Ratio based on the Method by Spakovszky et al.

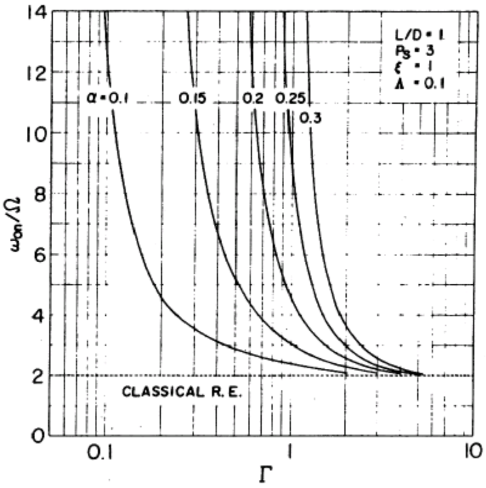

(a) Effect of α and Γ

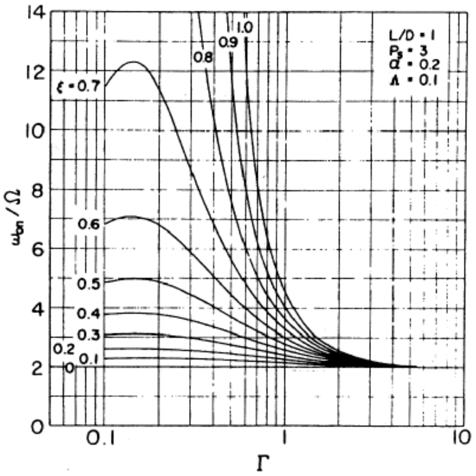

(b) Effect of ξ and Γ

Figure 4-18: Whirl Ratio by Analysis including Compressibility by Mori et al [16, 17].

4.4 Resonance

4.4.1 Calculation Method

In this chapter, the rotor dynamics of the bearing is theoretically considered. The rotor-bearing system of this bearing rig is modeled as shown in Fig. 4-19. Assuming that no external force and no damping force is applied to the shaft, the equation of motion of the shaft is given by

$$m\ddot{x} = -k_1x_1 - k_2x_2 \tag{4.4.1}$$

$$m\ddot{y} = -k_1y_1 - k_2y_2 \tag{4.4.2}$$

$$I\ddot{\theta}_x + I_p\omega\dot{\theta}_y = -l_1k_1x_1 + l_2k_2x_2 \tag{4.4.3}$$

$$I\ddot{\theta}_y + I_p\omega\dot{\theta}_x = -l_1k_1y_1 + l_2k_2y_2 \tag{4.4.4}$$

where,

(x, y)	Position of the mass center of the rotor, G, on the plane perpendicular to the rotational axis
(x_1, y_1)	Center position of the shaft supported by the compressor-side bearing
(x_2, y_2)	Center position of the shaft supported by the turbine-side bearing
l_1	Distance between the compressor-side bearing and G
l_2	Distance between the turbine-side bearing and G
(θ_x, θ_y)	Tilting angle of the inertial axis of the shaft
I_p	Inertia of the rotor about the rotational axis
I	Inertia of the rotor about the x- or y-axis
k_1	Spring constant of the turbine-side bearing
k_2	Spring constant of the compressor-side bearing

Among (x, y), (x_1, y_1), (x_2, y_2), l_1, l_2, and (θ_x, θ_y), the following relationships are found.

$$x_1 = x + l_1\theta_x , \tag{4.4.5}$$

$$y_1 = y + l_1\theta_y , \tag{4.4.6}$$

$$x_2 = x - l_1\theta_x \text{ and,} \tag{4.4.7}$$

$$y_2 = y - l_2\theta_y . \tag{4.4.8}$$

By substituting Eq. (4.4.1)-(4.4.4) by Eq. (4.4.6)-(4.4.9), we obtain

$$m\ddot{x} + \alpha x + \gamma\theta_x = 0 , \tag{4.4.9}$$

$$m\ddot{y} + \alpha y + \gamma\theta_y = 0 , \tag{4.4.10}$$

$$I\ddot{\theta}_x + I_p\omega\dot{\theta}_y + \gamma x + \delta\theta_x = 0 \text{ and} \tag{4.4.11}$$

$$I\ddot{\theta}_y - I_p\omega\dot{\theta}_x + \gamma y + \delta\theta_y = 0 , \tag{4.4.12}$$

where

$$\alpha = k_1 + k_2 , \tag{4.4.13}$$

$$\gamma = k_1 l_1 - k_2 l_2 \text{ and} \tag{4.4.14}$$

$$\delta = k_1 l_1^2 + k_2 l_2^2 . \tag{4.4.15}$$

Considering the axial symmetry of the rotor-bearing system, x and y, and θ_x and θ_y have the same amplitude and counter phase. Thus, we can assume the following free-oscillation answers of Eq. (4.4.9)-(4.4.12).

$$x = A\cos(pt+\beta)\,, \tag{4.4.16}$$

$$y = A\sin(pt+\beta)\,, \tag{4.4.17}$$

$$\theta_x = B\cos(pt+\beta) \text{ and} \tag{4.4.18}$$

$$\theta_y = B\sin(pt+\beta)\,. \tag{4.4.19}$$

By substituting Eq. (4.4.9)-(4.4.12) by Eq. (4.4.16)-(4.4.19) and comparing the coefficients of the trigonometrical functions, we finally obtain

$$f(p) \equiv (\alpha - mp^2)(\delta + I_p\omega p - Ip^2) - \gamma^2 = 0\,. \tag{4.4.20}$$

This equation gives the resonant frequency of the rotor-bearing system.

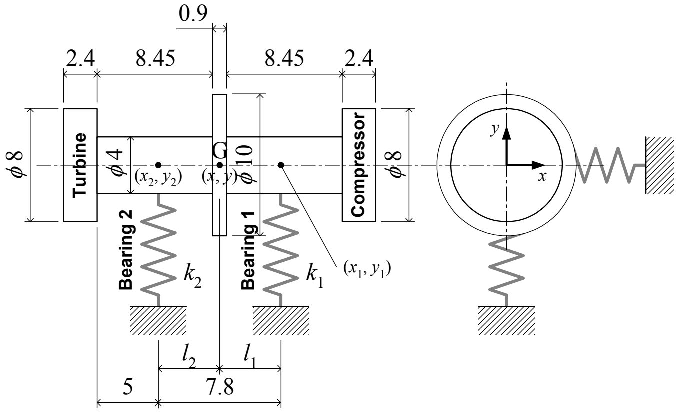

Figure 4-19: Calculation Model of the Rotor-Bearing System.

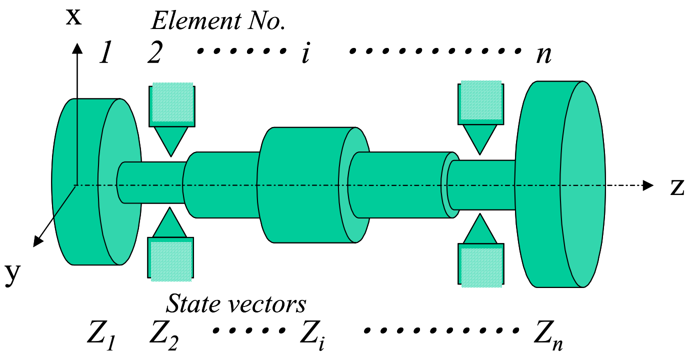

Figure 4-20: Cylinder Model for Transfer Matrix.

4.4.2 Transfer Matrix Method

More generally, transfer matrix method is used for the resonance speed analysis of the rotor. This method discretizes the rotor by many cylinders as shown in Figure 4-20, and models the structure dynamics property of each cylinder element by transfer matrix. Then the state vector

$$Z = \begin{bmatrix} x & \theta_x & M_x & -V_x & -y & \theta_y & M_y & V_y & 1 \end{bmatrix}^T \tag{4.4.21}$$

of the nth element is calculated as,

$$Z_n = \prod_{i=1}^{n} T_i Z_0 . \tag{4.4.22}$$

Here, T_i is the transfer matrix of the ith element defined as,

$$T_i = T_{Ki} T_{Mi} T_{Bi} . \tag{4.4.23}$$

Three matrices in the right hand side are as follows.

Mass matrix;

$$T_{Mi} = \begin{bmatrix} 1 & 0 & 0 & 0 & 0 & 0 & 0 & 0 & 0 \\ 0 & 1 & 0 & 0 & 0 & 0 & 0 & 0 & 0 \\ 0 & -I_d\omega^2 & 1 & 0 & 0 & jI_p\Omega\omega & 0 & 0 & 0 \\ m\omega^2 & 0 & 0 & 1 & 0 & 0 & 0 & 0 & \Delta V_x \\ 0 & 0 & 0 & 0 & 1 & 0 & 0 & 0 & 0 \\ 0 & 0 & 0 & 0 & 0 & 1 & 0 & 0 & 0 \\ 0 & jI_p\Omega\omega & 0 & 0 & 0 & -I_d\omega^2 & 1 & 0 & 0 \\ 0 & 0 & 0 & 0 & m\omega^2 & 0 & 0 & 1 & -\Delta V_y \\ 0 & 0 & 0 & 0 & 0 & 0 & 0 & 0 & 1 \end{bmatrix} \tag{4.4.24}$$

Stiffness matrix;

$$T_{Ki} = \begin{bmatrix} 1 & l & l^2/2EI & \frac{l^3}{6EI} - \frac{l}{GA} & 0 & 0 & 0 & 0 & 0 \\ 0 & 1 & l/EI & l^2/2EI & 0 & 0 & 0 & 0 & 0 \\ 0 & 0 & 1 & l & 0 & 0 & 0 & 0 & 0 \\ 0 & 0 & 0 & 1 & 0 & 0 & 0 & 0 & 0 \\ 0 & 0 & 0 & 0 & 1 & l & l^2/2EI & \frac{l^3}{6EI} - \frac{l}{GA} & 0 \\ 0 & 0 & 0 & 0 & 0 & 1 & l/EI & l^2/2EI & 0 \\ 0 & 0 & 0 & 0 & 0 & 0 & 1 & l & 0 \\ 0 & 0 & 0 & 0 & 0 & 0 & 0 & 1 & 0 \\ 0 & 0 & 0 & 0 & 0 & 0 & 0 & 0 & 1 \end{bmatrix} \tag{4.4.25}$$

Spring & Damping matrix (only for the element with the bearing);

$$T_{Ki} = \begin{bmatrix} 1 & 0 & 0 & 0 & 0 & 0 & 0 & 0 & 0 \\ 0 & 1 & 0 & 0 & 0 & 0 & 0 & 0 & 0 \\ 0 & 0 & 1 & 0 & 0 & 0 & 0 & 0 & 0 \\ -(k_{xx} + jc_{xx}) & 0 & 0 & 1 & k_{xy} + jc_{xy} & 0 & 0 & 0 & 0 \\ 0 & 0 & 0 & 0 & 1 & 0 & 0 & 0 & 0 \\ 0 & 0 & 0 & 0 & 0 & 1 & 0 & 0 & 0 \\ 0 & 0 & 0 & 0 & 0 & 0 & 1 & 0 & 0 \\ k_{yz} + jc_{yz} & 0 & 0 & 0 & -(k_{yy} + jc_{yy}) & 0 & 0 & 1 & 0 \\ 0 & 0 & 0 & 0 & 0 & 0 & 0 & 0 & 1 \end{bmatrix} \tag{4.4.26}$$

where,

k_{xy} = Spring constant, c_{xy} = Damping constant

E = Young's modulus, G = modulus of rigidity,

I_d *and* I_p = moment of inertia around the rotating axis and x or y axis,

A = cross sectional area, l = length of the element,

m = mass, ε = moment arm length of the unbalance, ϕ = phase angle of unbalance,

ω = angular velocity of whirling motion, Ω = angular velocity of shaft rotation,

Exciting for by unbalance $$\Delta V_x = m\varepsilon\omega^2(\sin\phi - j\cos\phi) \tag{4.4.27}$$

$$\Delta V_y = m\varepsilon\omega^2(\cos\phi + j\sin\phi) \tag{4.4.28}$$

4.4.3 Analysis of the Resonance Speed

Based on the calculation result of the hydroinertia bearing shown in Figure 4-21, calculation of the critical speed at the bearing clearance 30 µm is shown as an example. The bearing rigidity is calculated from the rate of the change of load capacity by changing the eccentricity at the bearing clearance of 30µm. It is 0.071 N/µm in current case as shown in Figure 4-22. Using Eq. (4.4.20), the resonant speeds are estimated at 39,000 rpm for conical mode and 75,000 rpm for cylindrical mode.

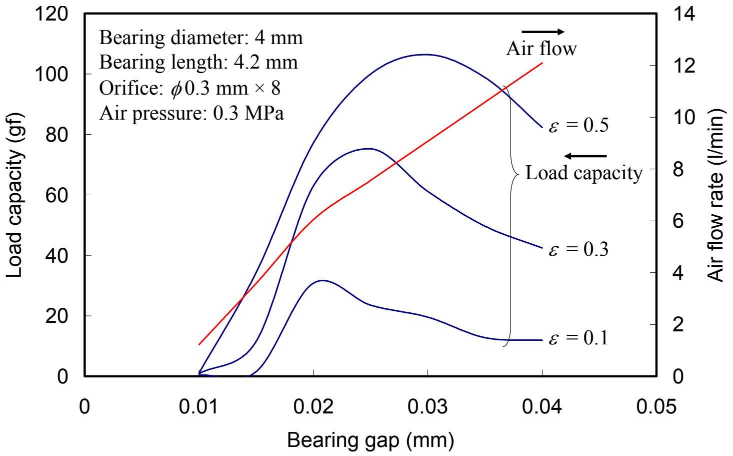

Figure 4-21: Load Capacity and Air Flow Rate as Functions of the Bearing Gap.

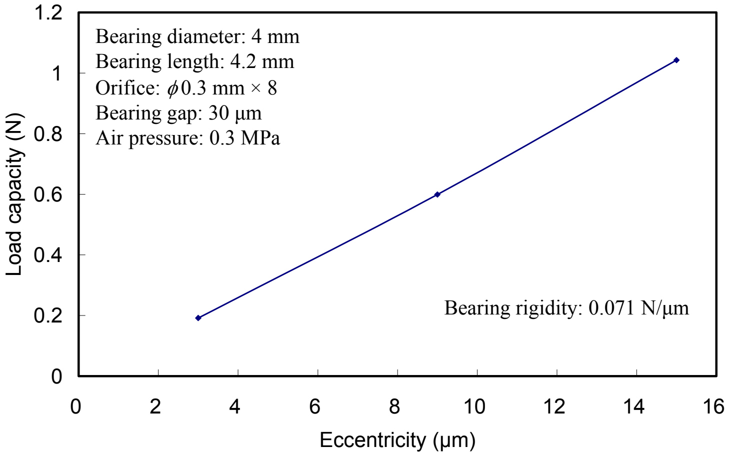

Figure 4-22: Relationship between the Eccentricity and the Load Capacity.

The rotor has two rigid mode resonance speeds below the designed operation speed. Hence, the rotor has to pass through those resonance points during the start up operation. To successfully pass through the resonance points, the rotor is required to be well balanced so that it will not vibrate at the amplitude larger than the bearing clearance at the resonance speed, to prevent the rotor to hit the bearing. Hence, the estimation of the vibration amplitudes at the first two resonance frequencies is required.

Theoretical estimation of the resonant peaks of the rotor to assess the easiness to pass the resonant speeds is attempted. The equation of motion of the rotor with eccentricity e and inertial tilting τ (the phase difference between e and τ is β) is given by replacing x, y, θ_x and θ_y in Eq. (4.4.9)-(4.4.12) as

$$x \to x + e\cos\omega t\,, \tag{4.4.29}$$

$$y \to y + e\sin\omega t\,, \tag{4.4.30}$$

$$\theta_x \to \theta_x + \tau\cos(\omega t + \beta) \text{ and} \tag{4.4.31}$$

$$\theta_y \to \theta_y + \tau\sin(\omega t - \beta)\,. \tag{4.4.32}$$

Eventually, we obtain

$$m\ddot{x} + \alpha x + \gamma\theta_x = \underline{me\omega^2\cos\omega t}\,, \tag{4.4.33}$$

$$my + \alpha y + \gamma\theta_y = \underline{me\omega^2\sin\omega t}\,, \tag{4.4.34}$$

$$I\ddot{\theta}_x + I_p\omega\dot{\theta}_y + \gamma x + \delta\theta_x = \underline{\underline{(I_p - I)\tau\omega^2\cos(\omega t + \beta)}} \text{ and} \tag{4.4.35}$$

$$I\ddot{\theta}_y + I_p\omega\dot{\theta}_x + \gamma y + \delta\theta_y = \underline{\underline{(I_p - I)\tau\omega^2\sin(\omega t + \beta)}}\,. \tag{4.4.36}$$

The single-underlined parts represent oscillating force by e, and the double-underlined parts represent that by τ. Assuming rotation-synchronous whirl as the answers of Eq. (4.4.33)-(4.4.36), we calculate the amplitude of the oscillation of the rotor. The oscillation by e are given by

$$x = P\cos\omega t\,, \tag{4.4.37}$$

$$y = P \sin \omega t \,, \tag{4.4.38}$$

$$\theta_x = P' \cos \omega t \ \text{ and} \tag{4.4.39}$$

$$\theta_y = P' \sin \omega t \,. \tag{4.4.40}$$

By comparing the coefficients of the trigonometrical functions, the amplitudes *P* and *P'* are expressed as

$$P = \frac{m\omega^2 \left\{ \delta - (I_p - I)\omega^2 \right\} e}{f(\omega)} \ \text{ and} \tag{4.4.41}$$

$$P' = \frac{-m\omega^2 \gamma e}{f(\omega)} \tag{4.4.42}$$

Also, the oscillation by τ are given by

$$x = Q \cos(\omega t + \beta) \,, \tag{4.4.43}$$

$$y = Q \sin(\omega t + \beta) \,, \tag{4.4.44}$$

$$\theta_x = Q' \cos(\omega t + \beta) \ \text{ and} \tag{4.4.45}$$

$$\theta_y = Q' \sin(\omega t + \beta) \,. \tag{4.4.46}$$

In similar method, the amplitudes *Q* and *Q'* are expressed as

$$Q = \frac{-(I - I_p)\omega^2 \gamma \tau}{f(\omega)} \ \text{ and} \tag{4.4.47}$$

$$Q' = \frac{(I - I_p)\omega^2 (\alpha - m\omega^2)\tau}{f(\omega)} \,. \tag{4.4.48}$$

Because Eq. (4.4.33)-(4.4.36) are linear equations, the oscillation of the rotor is the summation of Eq. (4.4.37)-(4.4.40) and Eq. (4.4.43)-(4.4.46). The oscillation at the bearing are obtained using Eq. (4.4.5)-(4.4.8).

Figure 4-23 and 4-24 show the amplitude of the rotation-synchronous oscillation near the resonant speeds. Unbalance of 0.2 g·µm and 1 g·µm are assumed for Fig. 4-23 and 4-24, respectively. It is clear that the smaller unbalance is preferred to pass the resonant speeds. For an externally-pressurized air bearing with a large bearing gap (20-30 µm), the resonant peaks shown in Fig. 4-23 and 4-24 are not so problematic to pass, but they are severe for a hydrodynamic air bearing with a small bearing gap (several µm). To make the unbalance small, a half-cut bearing, which does not need the reassembly of the rotor to be inserted, will be effective.

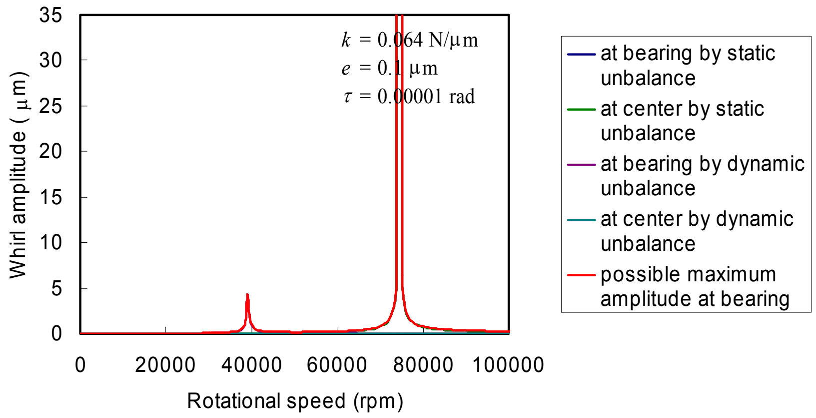

Figure 4-23: Amplitude of the Rotation-Synchronous Oscillation by an Unbalance of 0.2 g·μm.

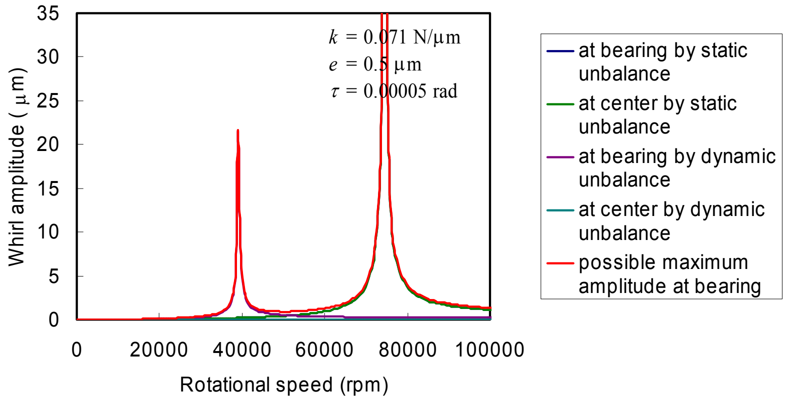

Figure 4-24: Amplitude of the Rotation-Synchronous Oscillation by an Unbalance of 1 g·μm.

However, the practical estimation of the vibration amplitude at the resonance frequencies is difficult because the calculation is largely affected by the damping and the dynamic response, and it is difficult to estimate the models of these values, accurately.

A useful guideline in such a case is to use the "G grade" defined in Japan Industrial Standard (JIS) as "Rotating Machines – Balancing requirements of rigid rotors; JIS-B0905". The value of the "G grade" is defined as,

$$G = e\,\omega \tag{4.4.49}$$

$$= e\,n / 9.55 \tag{4.4.50}$$

where, e is the distance between the center of the gravity and the geometric center of the shaft in mm, ω is the shaft speed in rad/sec, and n is the shaft speed in rpm. This relation is also shown in Figure 4-25. The required "G grade" for gas turbines is usually set around 2.5 to 6.3. Hence, the rotor to operate at 890,000 rpm is required to have the e of 0.027μm for G=2.5, and 0.068μm for G=6.3.

The weight of the rotor is 2.3g at current configuration. Therefore, the required static unbalance is 0.062g-μm for G=2.5, and is 0.16g-μm for G=6.3. Hence, it is found that unbalance of about 0.1g-μm is required to achieve the balance level required for the large gas turbines.

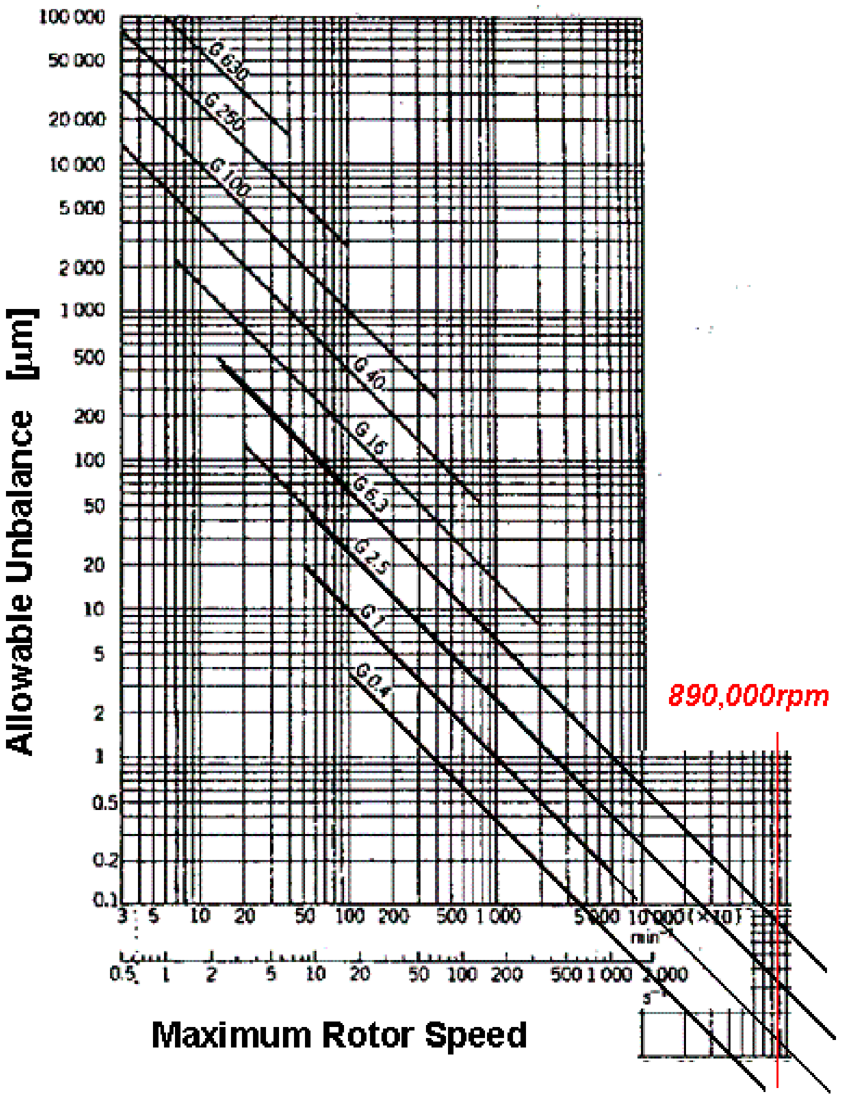

Figure 4-25: The "G Grade" Diagram by JIS-B0905.

4.4.4 Balancing Method and the Achieved Unbalance Level

A special balancer has been developed to achieve the required rotor balance of 0.1g-μm. The developed balancer is shown in Figure 4-26 and Figure 4-27. A conventional belt-drive type balancer has been used as the base for the balancer for current micro-rotor because it has flexibility in modifying the system. The material of the V-shape rotor supports have been changed to Poly-Ether Ether-Ketone (PEEK) plastic because of its durability, low friction, and softness that prevent damaging the rotor shaft. The support made of aluminum will easily damage the shaft. Also, the high friction by aluminum generates relatively large vibration that increases the noise level of the load sensor output signal. The V-support made by aluminum is also easy to wear. When it is worn, the contact area between the V-support and the shaft increases, and it becomes difficult to keep the constant rotational speed required for the accurate balancing. The support made by TFPT, which is well known as Teflon, has a very low friction coefficient, but wears fast, and it is difficult to keep the constant shaft speed. In addition to this change of the material of the V-support, increase of the sensitivity of the shaft unbalance measurement has been achieved by increasing the output signal gain of the load cells, and increasing the shaft rotational speed. With this balancing machine, the required rotor unbalance as small as 0.1 g-μm has been achieved.

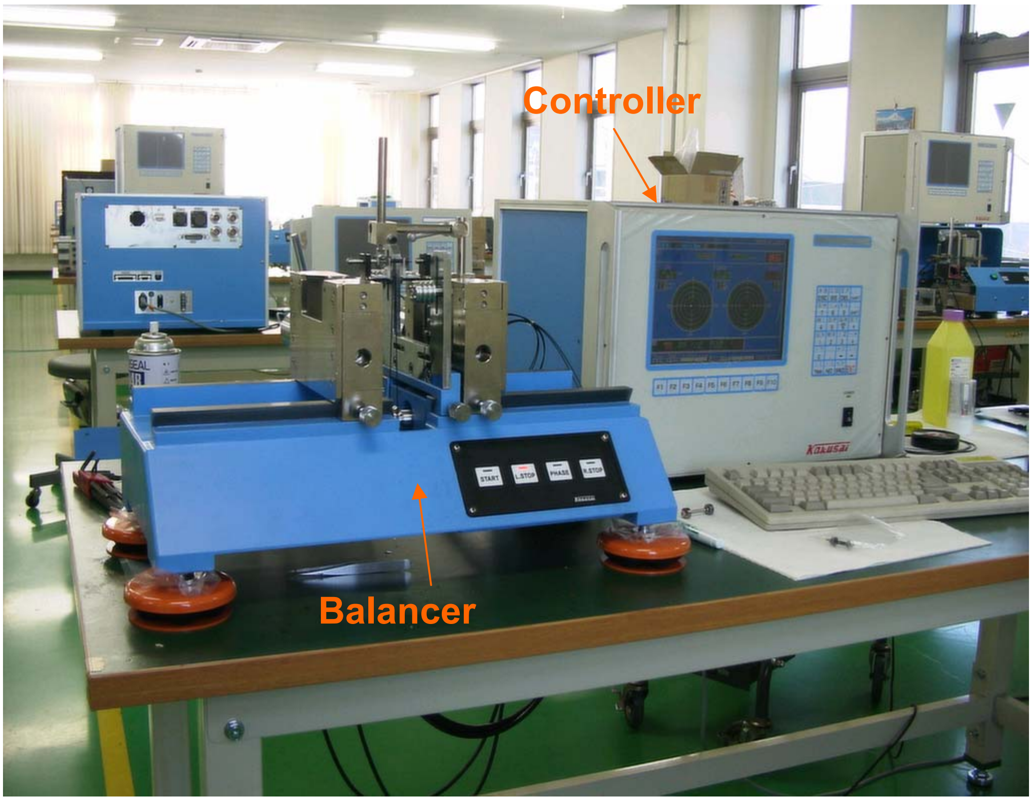

Figure 4-26: The Micro-Balancer Developed for Micro-High-Speed Rotor.

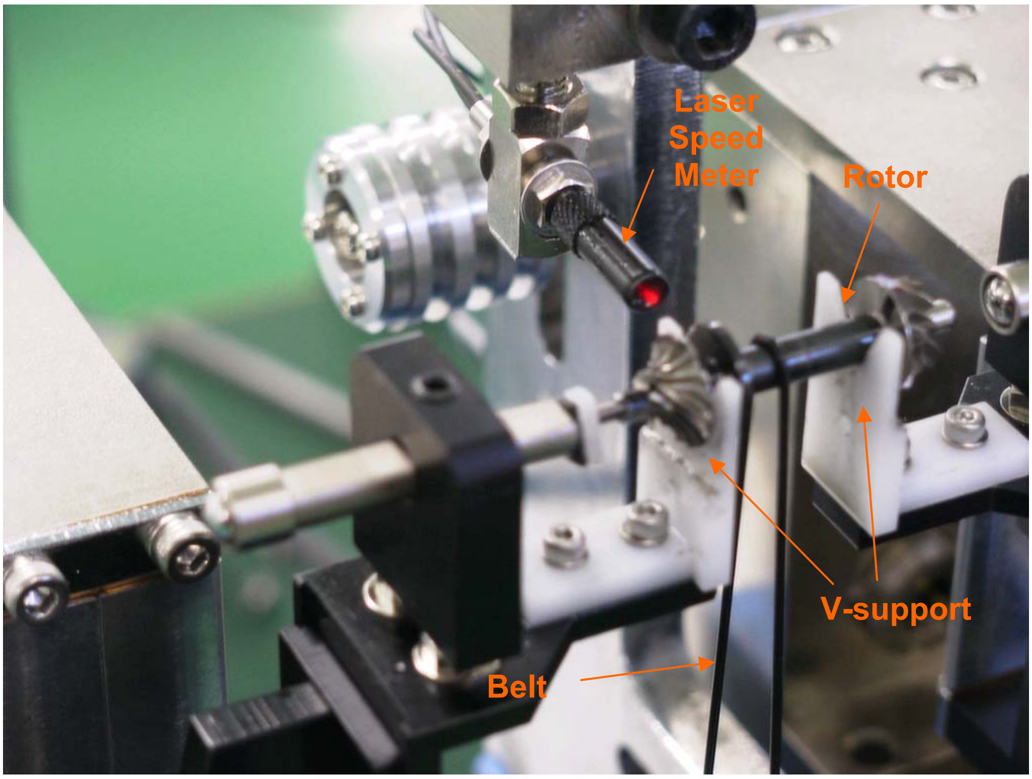

Figure 4-27: The Close-Up View of the Micro-Balancer.

The dynamic rotor balance was measured at 8500rpm plus minus 5rpm, and adjusted at two surfaces; one at the back face of the turbine impeller, and the other at the back face of the dummy compressor. The adjustment was done by a high-speed hand-held grinder called Leuter, with a diamond grindstone.

Current balancer requires the special skill of the operators. The balancer and the balancing method should by further developed to make the balancing job easier and less stressful, in future.

5.0 MICRO-BEARING TEST

5.1 Development of the Micro-Bearing Tester

5.1.1 Design

A micro-bearing tester has been designed and fabricated. The bird eye views and the cross sectional view of the tester are shown in Figure 5-1 and 5-2, respectively, and the micro-rotor is shown in Figure 5-3. The rotor of diameter 4mm has a thrust disk of diameter 10mm at the center of the shaft, with two journal bearings on the shaft, each at the symmetric position to the thrust disk. The rotor is driven by a centrifugal turbine of diameter 10mm, which is located at an end of the shaft, and a dummy compressor is located at the other end of the shaft. The dummy compressor is a cylindrical shaft that is designed to have the same mass and moment of inertia to the compressor for the expected micro-machine gas turbine hence the rotor has the same rotor dynamic characteristic to the rotor for the gas turbine.

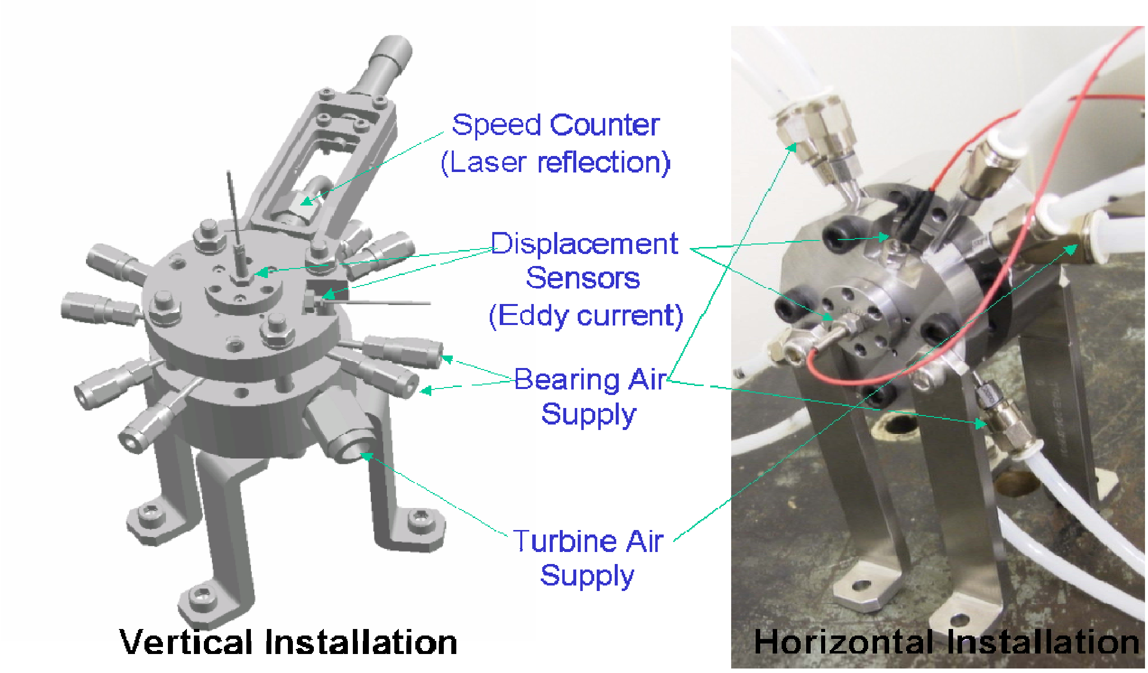

Figure 5-1: Bird-Eye View of the Micro-Bearing Tester.

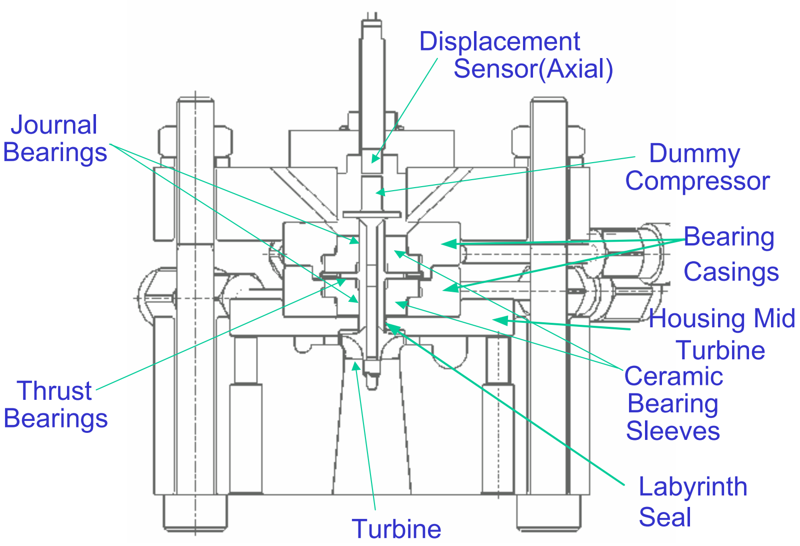

Figure 5-2: Cross Sectional View of the Micro-Bearing Tester.

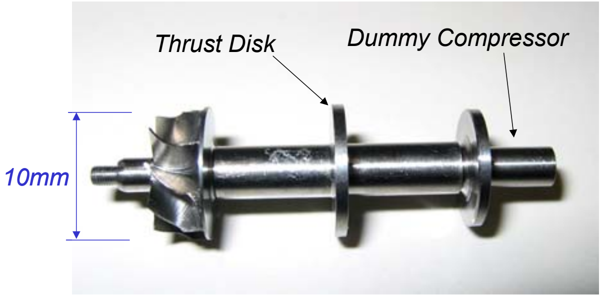

(a) Hydroinertia gas bearings

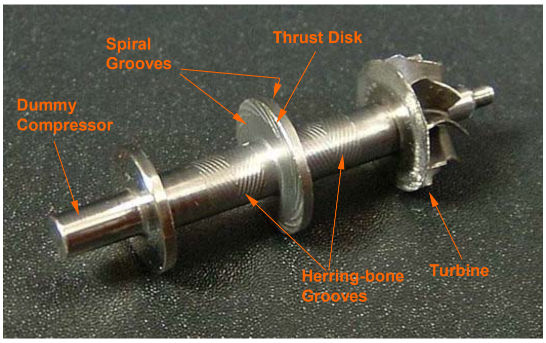

(b) Herring-bone & Spiral groove hydrodynamic gas bearings

Figure 5-3: The Assembled Rotor of the Micro-Bearing Tester.

The rotor has a conventional structure of high-speed turbo machines that the shaft and the impeller are connected by a tie-bolt. The diameter of the tie-bolt is 1.6mm. The rotor is made of titanium (Ti-6Al-4V), and weighs 2.3g. The shaft is coated by CrN ceramic of 3μm thick to increase the durability in the case that the rotor touches the bearing sleeve during the operation.

The bearing sleeves are made of Zirconium (ZrO2) ceramic. The selection of Zirconium ceramic is also to increase the durability of the bearing sleeves in the event of the rotor touching the bearing sleeves. The bearing will easily be burnt even by a slight contact of the rotor and the bearing sleeves, if both sides are not made of ceramics. Each bearing has 8 holes of diameter 0.3mm to feed the bearing gas. The supply pressure can be changed independently for each bearing.

The bearing unit is contained in the housing unit that also contains the turbine nozzles, scroll, and labyrinth seal to separate the pressure at the bearing and the turbine. The parts of the housings and the bearing assembly are shown in Figure 5-4 and Figure 5-5, respectively.

The maximum loading of the journal bearing will be obtained at about 30 μm of the bearing clearance for the journal bearings, and at about 20 μm of the bearing clearance for the thrust bearings. The bearing clearance of the thrust bearing can be changed by changing the thickness of the spacer ring located between two pairs of ceramic bearing sleeves. The radial clearance of the journal bearings can be changed by replacing the shaft to that of different diameter.

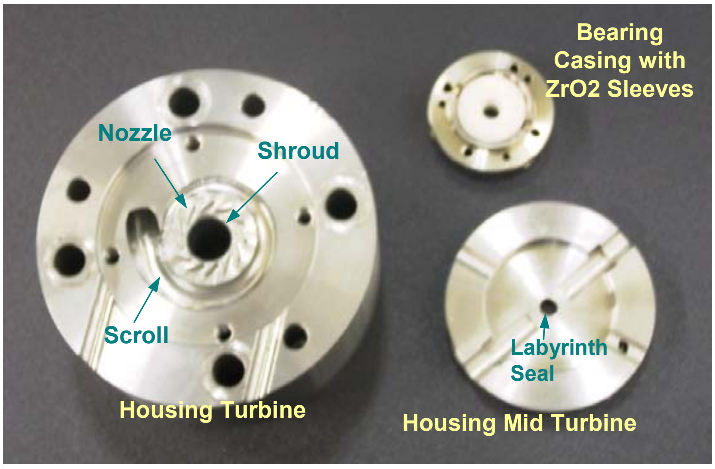

(a) Housings in turbine-side

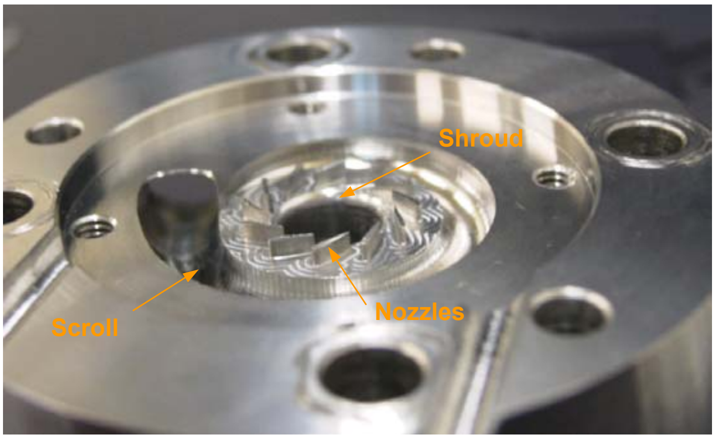

(b) Turbine scroll

(Figure 5-4 continued on next page).

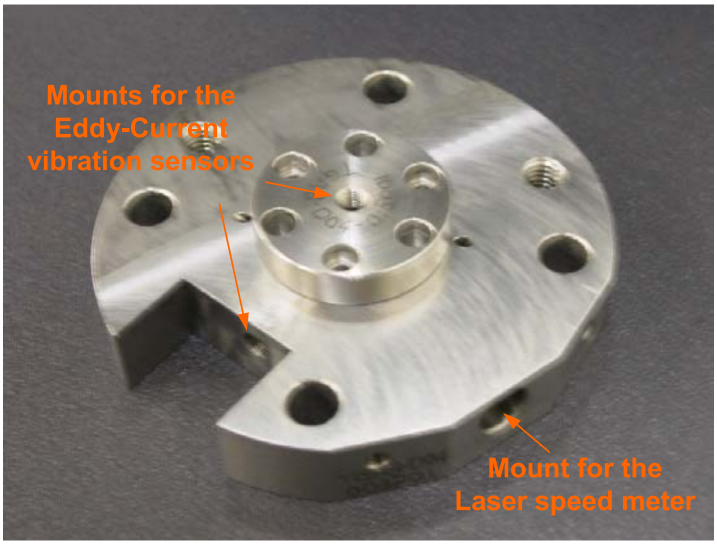

(c) Mount for sensors

Figure 5-4: Housings of the Micro-Bearing Tester.

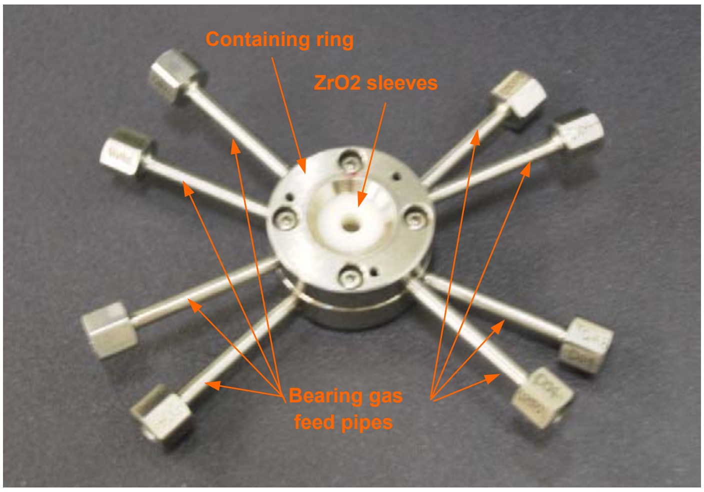

Figure 5-5: Bearing Assembly.

The micro-bearing tester has been designed under following requirements.

(1) The rotor vibration in axial and radial direction should be measured at an accuracy of 1μm.

(2) The rotor should simulate the rotor dynamics of the micro-turbo charger rotor for 100W micromachine gas turbine.

(3) The rotor should be able to be assembled in the tester without changing the balance level after balancing it to 0.1g-μm.

(4) The supply pressure of the journal bearings and the thrust bearings can be altered independently.

(5) The bearing clearances and the supply pressure can be altered for the parametric tests.

(6) The tip clearance (in axial direction) can be adjusted.

(7) The bearings validated in this tester should be able to be transplanted to the micro-turbo charger for the compressor aerodynamic test.

(8) The roundness and the alignment of the journal bearings should be less than 5μm.

(9) The flatness of the thrust bearing should be less than 3μm.

These requirements are implemented in the design as follows.

(1) The rotor vibrations are measured at 2 locations. The measurement of the radial vibration should be made at the location that the largest amplitude along the rotor will emerge. From the vibration character of the rotor, the frequency of the 3rd mode, which is the first bending mode, is larger than the maximum shaft rotation frequency. Hence, only the first two solid vibration modes, namely, the conical mode and the cylindrical mode, will be considered. For these two modes, the largest radial amplitude appears at the end of the shaft, which is the location of either turbine impeller or compressor impeller. The vibration at these locations are also very important because they define the required tip clearance to prevent crashing of the impeller tip with the shroud, while from the aerodynamic point of view a smaller as possible tip clearance is desirable to minimize the efficiency drop of the compressor and the turbine.

To realize the vibration measurement at required accuracy, the eddy current type displacement sensors have been selected. The selected sensor and its linearity are shown in Figure 5-6 and 5-7, respectively, and their specifications are tabulated in Table 5-1. The diameter of the sensing head is 3mm, and the sensor requires a 3mm wide surface on the rotor facing to the sensor head, and the similar size of open space around the sensor head. Since, such a surface can be found on neither the compressor nor on the turbine, and since the turbine cannot be removed because it is driving the shaft, the compressor impeller has been replaced by a cylindrical shape dummy compressor.

Figure 5-6: The Eddy Current Gap Sensor used in the Tester.

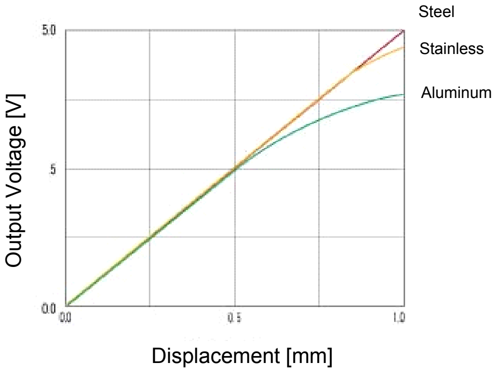

Figure 5-7: The Linearity Data of the Eddy Current Gap Sensor.

Table 5-1: Specification of the Eddy Current Displacement Sensor and the Amp

Eddy current displacement sensor 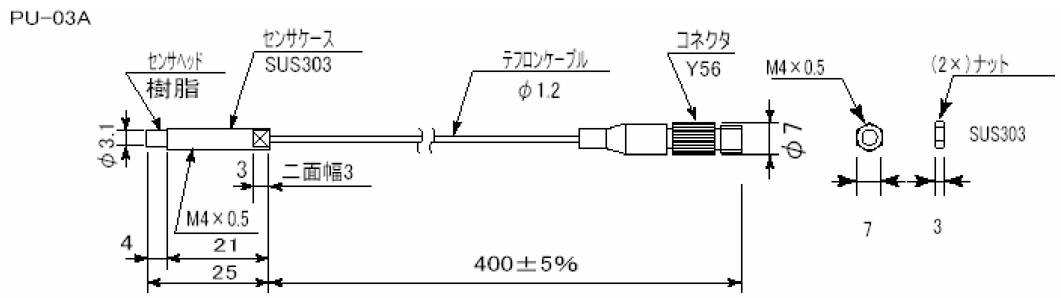 	
Makes	AEC
Type	5503A
range	0-1.0mm
Output voltage @ amp. exit	0-5V
Sensitivity	0.2mm/V
Resolution	0.5μm
Linearity	1%
Temperature range	−20℃～+180℃
Temperature effect	±0.8μm/℃ at −20℃～0℃ ±0.6μm/℃ at 0℃～+180℃
Amplifier	
Type	AEC-5503
Frequency response	-2dB @ 0 – 20kHz
Temperature effect on the Gain	plus minus 0.1%/degC

Usually, two sensors are used to measure the radial displacement to distinguish conical mode and cylindrical mode. However, due to the limit of the space, only one sensor is used at one end of the rotor. Since the vibration mode of current interest is limited to the first two rigid modes, i.e. conical mode and cylindrical mode, the mode can be distinguished from the comparing the frequency to the calculation. If we use laser reflection type probe of diameter 0.8mm, which we used for the rotor speed measurement, we could install two probes for radial vibration measurement. However, reflection type sensor will largely be affected by the nonuniformity of the surface reflection rate, and is difficult to distinguish the vibration synchronous to the shaft speed.

The weakness of the eddy current sensor, other than the large size, is that the material to be measured is limited to magnetic materials. Hence, if the rotor is made of ceramics, other type of sensor, for example laser reflection type sensor, has to be used.

(2) The rotor consists of the same material, the same shaft dimension, the same turbine impeller, and the same tie bolt construction, but the compressor impeller of the rotor for the micro-turbo charger is replaced with a dummy compressor of the same mass and the same moment of inertia. The assembled rotor is shown in Figure 5-3, and the critical speeds at various bearing supply pressures are shown in Figure 5-8.

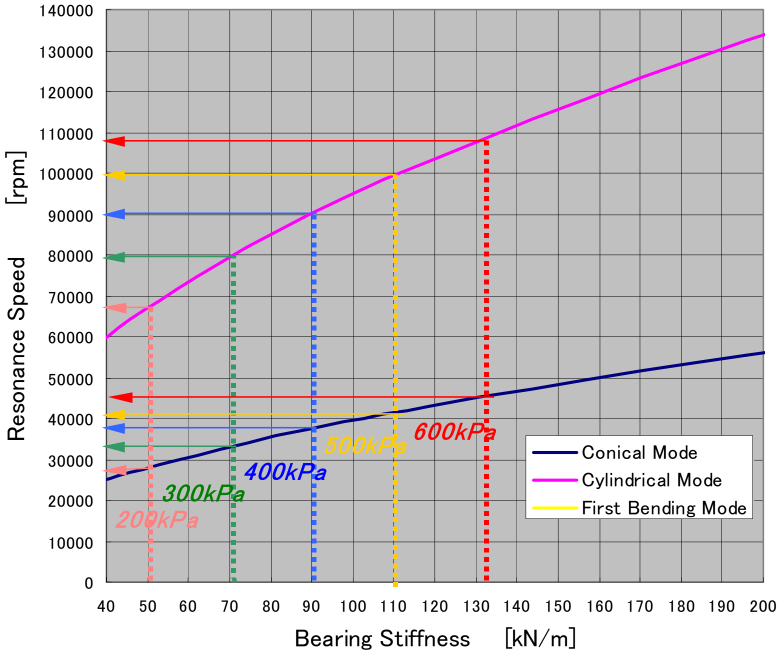

Figure 5-8: Critical Speed of the Rotor.

(3) To realize the assembling of the tester without changing the balance level of the rotor, the tie bolt structure of the rotor should not be reassembled after the balancing. Reassembling the rotor after the balancing will increase the 0.1g-µm of the unbalance achieved in the balancing to about 1g-µm. Since the geometry of the rotor is already defined as that shown in Figure 5-3 from the rotor dynamic requirement, the way to satisfy current requirement is to split the bearing. The difficulty in splitting the bearing is how to realize the geometrical accuracy of the air bearings that require very high accuracy of the roundness and flatness for the surface of the journal bearing and the thrust bearing, respectively. This issue has been overcome by a structure of fitting half-split bearings in a ring. This structure is shown in Figure 5-9 and 5-10. The bearing sleeves are made of ZrO_2 ceramics, and the container rings called “Bearing Casing” are made of stainless steel (SUS 403 in JIS Japan Industrial Standard).

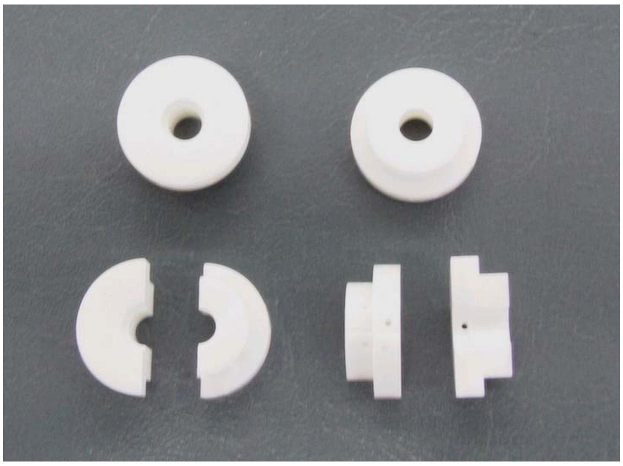

Figure 5-9: The Ceramic Bearing Sleeves made of ZrO_2 Ceramics (showing both half split sleeves and circular sleeves used for initial test).

(a) Dummy compressor side (male)

(b) Turbine side (female)

Figure 5-10: Half Split Ceramic Sleeves contained in a Bearing Casing.

(4) The gas supply system of the journal bearings and the thrust bearings were made separate to keep the capability of changing the two supply pressures independently. The bearing casing with the feeding pipe installed has already been shown in Figure 5-5.

(5) The bearing clearances of the thrust bearing was designed to be easily changeable by changing the thickness of the "Ring Spacer" to put in between both side of the bearing sleeves. For changing the clearance of the journal bearing, re-fabrication of either shaft or bearing sleeves are necessary.

(6) The tip clearance of the turbine in axial direction can be adjusted by altering the thickness of the "Housing Mid Turbine". If the tip clearance is too loose, it can be reduced by polishing the end surface of the "Housing Mid Turbine". If the tip clearance is too tight, it can be increased by adding shims in between the "Housing Mid Turbine" and the bearing casing. The "Housing Mid Turbine" is shown in Figure 5-11. This part also has a function by separating the bearing pressure and the turbine pressure by the labyrinth seals formed on the inner diameter. Since the inner diameter is 4mm, this part is also split in half to enable the assembly of the tester without removing the tie bolt of the rotor.

Figure 5-11: The Half Split "Housing Mid Turbine".

(7) Geometries of the shaft, the journal bearings, the thrust bearings, and the turbine are made identical to those of the micro-turbo charger test rig for micromachine gas turbine. The bearing can be directly transplanted to the micro-turbo charger for the compressor aerodynamic test, after the operation at the design speed of 870,000 rpm is achieved in the micro-high-speed bearing tester.

(8) 5μm of the bearing roundness has been achieved by the structure of containing the half split bearing sleeves in a containing ring called "Bearing Casing". The target clearance between the "Bearing Casing" and the sleeves is 2μm. The alignment of the journal bearings less than 5μm has been achieved by finishing the inner diameter of the journal bearings by polishing after the two "Bearing Casings", namely the male and the female, are connected.

(9) 1μm of the flatness has been achieved on the thrust bearing face by separating the bearing sleeves from the "Bearing Casing" and polishing a pair of sleeves using a special jig to keep the pair in contact.

5.1.2 Accuracy of the Fabrication

Most of the parts are made by machining. The parts that require especially high accuracy are the roundness and the alignment of the journal bearings, and the flatness of the thrust bearings. The accuracies of the fabricated journal bearings and the rotor shaft are shown in Table 5-2 and 5-3, respectively. The journal bearings are fabricated almost within the required accuracy. The thrust bearings were fabricated within required accuracy, but the thrust disk on the rotor showed large inaccuracy. The thrust disk showed difference between the thickness at the root and at the tip, as large as 14μm in some cases. More detailed measurements are required to reveal the detail of the inaccuracy, and find the fabrication procedure to prevent such an error to occur.

Table 5-2: Achieved Fabrication Accuracies of the Journal Bearings

Bld. #	Compressor side				Turbine side			
	Axial Position	Diameter Error	Roundness	Concentricity	Axial Position	Diameter Error	Roundness	Concentricity
	[mm]	[µm]	[µm]	[µm]	[mm]	[µm]	[µm]	[µm]
	requirement	3	5	5	requirement	3	5	5
1	12.5	-1	2.1	6.3	12.5	-3	1.8	1.4
	10	-2	1.7	5.0	10	-3	4.2	2.3
2	12.5	-2	8.2	6.9	12.5	-1	3.2	4.1
	10	0	1.9	6.0	10	+1	2.4	1.8

Table 5-3: Achieved Fabrication Accuracies of the Rotor Shaft

Bld. #	Shaft			Thrust Disk				
	Axial Position	Diameter Error	Roundness	Radial Position	Thickness Error			
				θ angle	0deg	90	180	270
		[µm]	[µm]	[mm]	[µm]	[µm]	[µm]	[µm]
	requirement	2	2	requirement	2	2	2	2
1	A	-0.5	0	Inner	+3	+3	+2	+1
	B	-1	0.5	Outer	-1	-1	-2	-3
	C	-1	0.5					
	D	-0.5	0.5					
2	A	-1	0.5	Inner	+10	+11	+14	+13
	B	-1.5	0.5	Outer	0	+1	0	0
	C	-1	0.5					
	D	0	0.5					

5.2 Micro-Bearing Tests

5.2.1 Test Setup

All the measurements made in the micro-bearing tester are listed in Table 5-5. The rotor speed is measured by optical displacement sensor of the diameter 0.8mm, shown in Figure 5-12. The test has been performed under the setup shown in Figure 5-13. The data acquisition software has been developed using a commercial software called LabView. The user interface of the developed program is shown in Figure 5-14. The rotor vibration data in axial and radial direction were sampled at 200kHz, which is 100kHz per channel.

Table 5-5: List of the Measured Data

Measured data		Quantity	Sensor	
			Type	Make & Type No.
Rotor Vibration	Axial	1	Eddy Current	AEC PU-03A(sensor)+5503A(amp)
	Radial	1		
Supply Gas Pressure	Thrust Bearing	1	Semiconductor	Copal Electronics PG-100-103GP 0-1000kPa(G) Accuracy: ±0.5%FS
	Radial Bearing	1		
Volume Flow Rate	Thrust Bearing Gas	1	Hot Wire	YAMATAKE CMS0050BPRN000000 Range:0-50 liter/min Accuracy: 0.5≦x ＜ 5L/min ±1%FS±1digit 5≦x≦50L/min ±3%RD±1digit
	Radial Bearing Gas	1		
	Turbine Air	1		STEC SEF-52 Range: 200 liter/min Accuracy: ±3%FS
Shaft Speed		1	Fiber-optic Laser Reflectance Dependent Sensor	Philtec D-20 Probe diameter 0.8mm Resolution:0.25μm @ DC-20KHz

Figure 5-12: Laser Displacement Sensor (ϕ0.8mm) used for Speed Measurement.

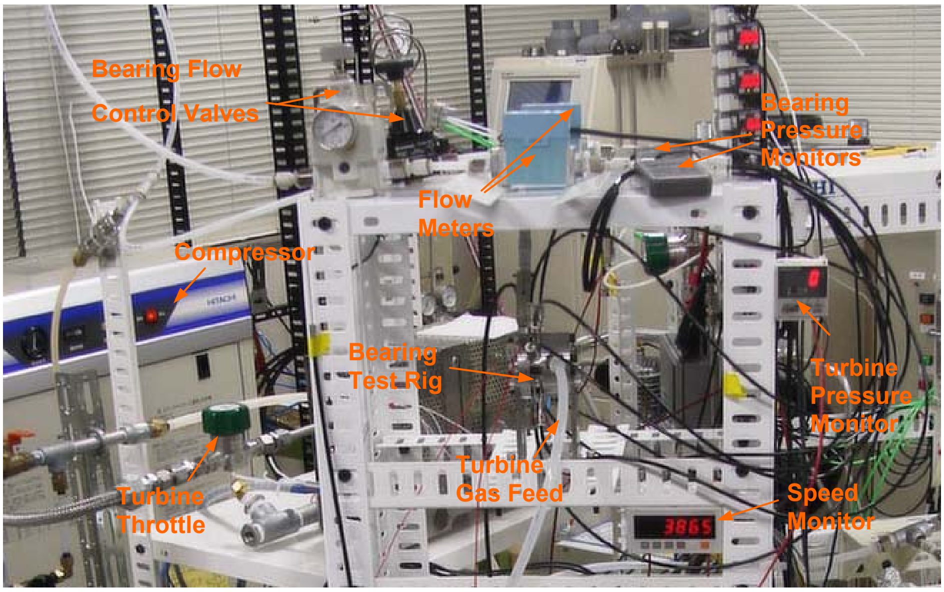

Figure 5-13: The Set Up of the Micro-Bearing Test.

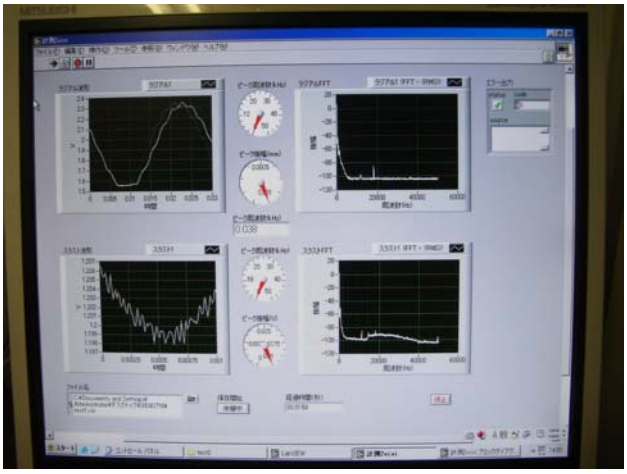

Figure 5-14: The User Interface of the Real-Time Data Acquisition System.

5.2.2 Hydroinertia Gas Bearing Test

The micro-bearing test of hydro-inertia gas bearing of shaft diameter 4mm has been performed. The shaft speed reached 770,000rpm, and crashed. The bearing supply pressure p_s was increased to 600kPa in this test. The rotor vibration data at various shaft speed between 670,000rpm and 770,000rpm are shown in Figure 5-15. Two dominant frequencies are seen in the figure; one at the frequency of the shaft rotational speed, and the other at a slower speed. The latter is the vibration due to whirl. The amplitude of the whirl is approximately 10μm. The variation of the vibration amplitude is shown in Figure 5-16. From the figure, it is presumed that both the amplitudes of the whirl and the rotor speed vibrations have grown large to cause the crash. The whirl frequency is approximately 1500 Hz, and is almost constant regardless of the shaft speed. The frequency of the whirl matches to the second resonance mode N_2, which is the cylindrical mode in this rotor. The whirl ratio is observed to be approximately 9 before the crash. The variation of the whirl ratio at various shaft speeds is shown in Figure 5-17. From the figure, it is conjectured that the whirl ratio of 11 is required to achieve the objective rotor speed of 870,000 rpm.

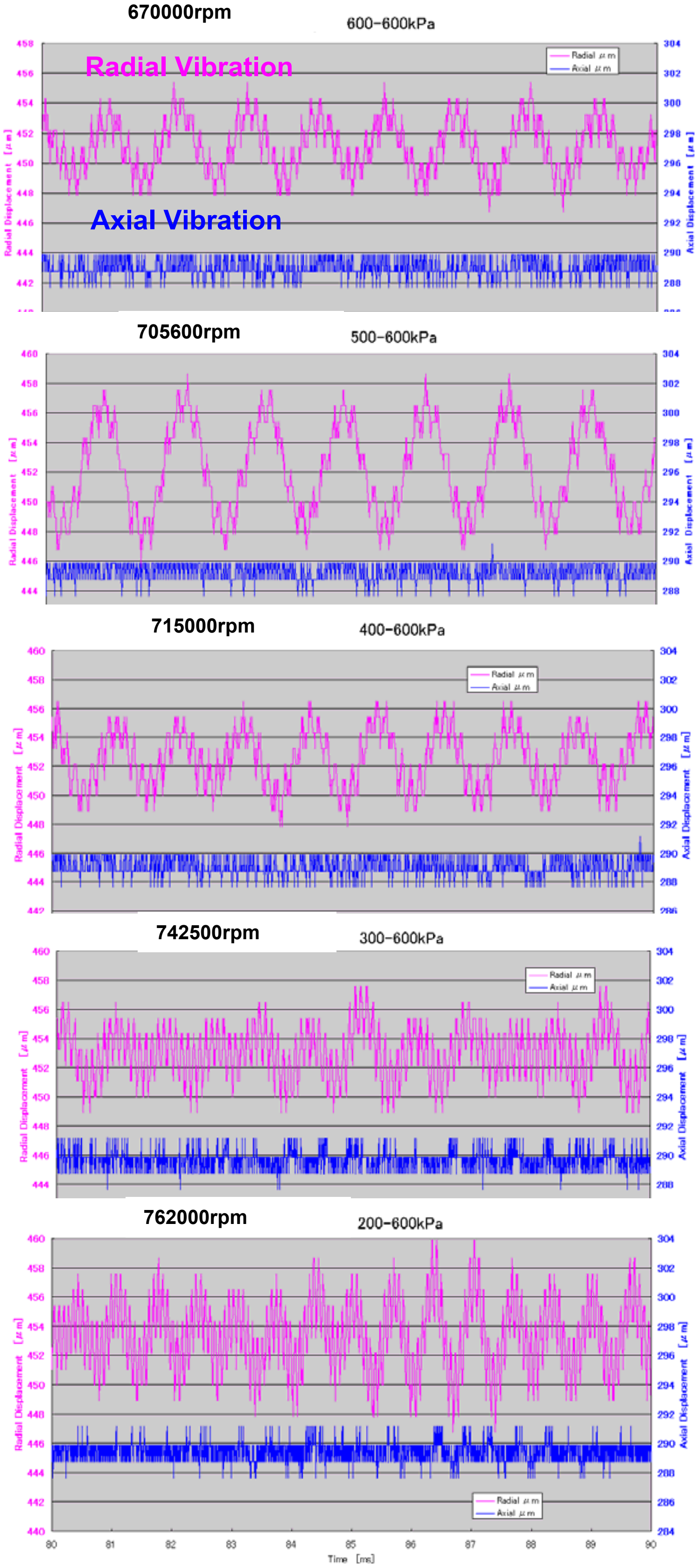

Figure 5-15: Shaft Vibration at Various Speeds.

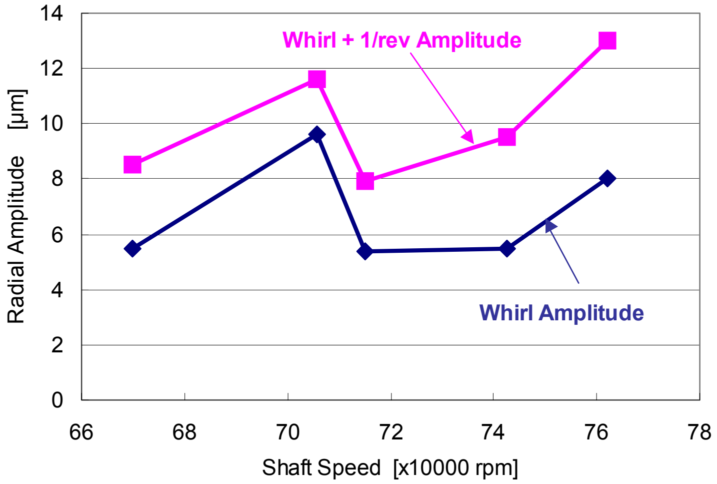

Figure 5-16: Amplitude of the Shaft Vibration at Various Speeds.

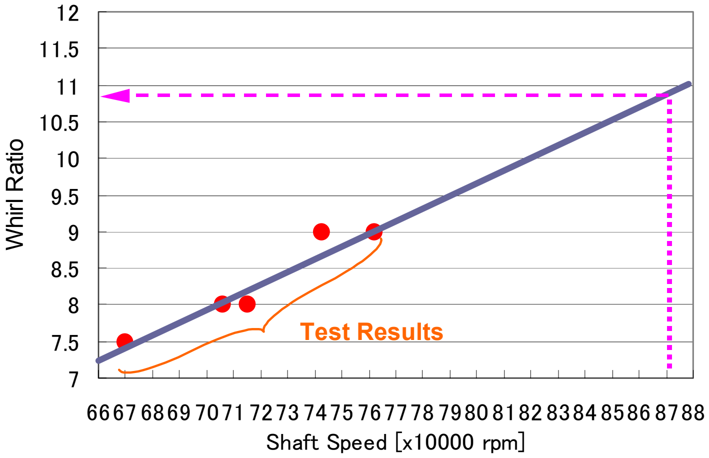

Figure 5-17: Whirl Ratio at Various Speeds.

The observed whirl ratio of 9 is very different from that of the micro-spinner, which was about 20. The whirl ratio became smaller than that of micro spinner because both the L/D and the stiffness *k* became larger. The whirl ratio of the gas bearing is known to be a function of radial bearing's stiffness. The bearing stiffness is the function of the bearing clearance *Cr*, bearing aspect ratio L/D, and the supply pressure p_s. The bearing clearance of the micro-spinner was almost the same to that of current bearing, but the supply pressure was lower, and the L/D was smaller.

In previous analysis by Spakovszky et al. shown in Figure 4-17, the whirl ratio of current dimension (L/D=1) is about 2 throughout various bearing. This does not match to current observation although the tendency of L/D effect does match. The analysis by Spakovszky includes the inertia effect of the bearing gas flow, but it assumes incompressible flow and also neglected the pressure gradient in tangential direction due to small L/D, in modeling the hydrodynamic stiffness due to viscous effect and pressure effect. Therefore, it is expected that the inclusion of the compressibility is important to analyze the flow in hydroinertia gas bearings. Hence, the test result is compared with the analysis result of Mori et al, shown in Figure 4-18, next. The design parameter Γ in the abscissa of the figure is calculated to be 0.43 for current case. Hence, it is found that the supply parameter α should be larger than 0.18 to achieve the whirl ratio larger than 11. However, α is already about 0.31 for the tested configuration, which suggests that the estimated value $\xi=1$ is incorrect, if the theory is correct. The ξ is a correction factor, which should only be found from matching to the experiment. To match the whirl ratio to the current test result of 6, ξ is found to be about 0.7 from Figure 4-18(b). Now, with ξ =0.7, α will needs to be about 0.45. This can be achieved by increasing the diameter or the number of the bearing gas supply holes. Careful studies will be needed to find the solution to achieve the increase of maximum speed, which is the product of resonance speed and whirl ratio. The increase of the diameter of the supply holes will reduce the stiffness of the bearing, and therefore, the resonance speed will be reduced. The increase of the whirl ratio should be large enough to gain an increase of the maximum speed even with the reduction of the resonance speed.

6.0 SUMMARY

6.1 What We Achieved

1) A new method to estimate the load capacity of the gas bearings including the compressible supersonic flow inside a hydroinertia gas bearing has been developed and validated by a corresponding experiment.

2) A method to analyse the whirl including the compressibility effect has been presented.

3) The rotordynamic requirements for the micro-rotor have been analysed. The rotor balance of 0.1g-mm has been realized by developing a micro-balancer, and by introducing the half-split bearing structure.

4) The hydroinertia gas bearing has been tested in a micro-spinner, and stably operated at 1,200,000rpm.

5) The analyses showed that hydroinertia gas bearings and hydrodynamic gas bearings, such as Herring-bone & Spiral groove bearings and foil bearings, are good candidates of bearings for micromachine gas turbines.

6) A micro-bearing test rig has been developed to test the bearings at a rotor dynamic configuration for micromachine gas turbine. The test rig has started its operation with both hydroinertia gas bearings and Herring-bone & Spiral groove hydrodynamic gas bearings, and the rotor vibration data have successfully been measured.

7) 770,000rpm has been achieved in the micro-bearing test of a rotor simulating that for micromachine gas turbine, using hydroinertia gas bearing of shaft diameter 4mm.

6.2 Remaining Issues

1) A method to increase the whirl stability of hydroinertia gas bearings should be established based on the analysis with compressibility effect, and should be validated by achieving 870,000 rpm in micro-bearing test.

2) The hydroinertia gas bearing test will be continued until 870,000 rpm is achieved.

3) The high precision fabrication methods will be studied to realize the required accuracy of the bearing parts, repeatedly.

4) The study on hydrodynamic gas bearings such as Herring-bone & Spiral groove bearings and foil bearings will be conducted to get quantitative data to compare with the hydroinertia gas bearings.

Nomenclature

A = flow area

A_e = flow area at the exit of the bearing

C = system damping force

C_D = discharge coefficient of the inherent orifice (= 0.85 in general)

C_r = radial clearance of radial bearing

c = flow coefficient of inherent orifice

D = shaft diameter

d , d_s = diameter of the bearing gas supply hole

e = Eccentricity of the rotor (Distance of the inertial center from the shape center of the shaft)

F = force generated by the impact of gas flow from the supply hole

h = bearing clearance

k = bearing stiffness = $k_s - j\, k_d$

k_s = bearing stiffness due to hydrostatic effect

k_d = bearing stiffness due to hydrodynamic effect = $k_p - k_v$

k_p = hydrodynamic bearing stiffness due to pressure effect

k_v = hydrodynamic bearing stiffness due to viscous effect

L = bearing length

L_a = half of the radial bearing exit width per supply hole = $\pi D/2n$

L_b = half of the bearing length = $L/2$

l_i = stream line length of the strips in developed surface of a radial bearing

M = Mach number

M_1, M_2 = Mach number ahead and behind the shock wave

M_e = Mach number at the exit of the bearing

m = hydraulic mean depth = $h/2$

m = mass of the rotor

m_w = mass per bearing

$\dot{m}$ = flow rate of the bearing gas

N = rotational speed

$N_{1,2}$ = the first and second resonance frequency

n = number of the supply holes

n_k = number of the supposed streamlines

p_1, p_2 = pressure ahead and behind the shock wave

P_a = ambient pressure

P_s = supply gas pressure

Q = volumetric flow rate of the bearing

$\mathcal{R}$ = gas constant

R = radius

R_0 = bearing radius

Re = Reynolds number

T = gas temperature

T_s = supply gas temperature

u = flow speed

W = load capacity

x = coordinate along the bearing radius of the circular thrust bearing

α = supply parameter defined by equation (4.3.18)

ε = eccentricity ratio

Γ = the designing parameter defined by equation (4.3.17)

κ = specific heat ratio

λ = coefficient of wall surface friction

μ = viscosity

ν = dynamic viscosity

θ = angle of the hypothetical circular thrust bearings

τ = Tilting angle of the inertial axis from the shape center of the shaft

ω = Angular velocity of the rotor

ξ, = correction factor for the effective pressure gradient in tangential direction

Ψ = correction factor for dispersion effect of discrete feed (= 0.8 in general)

REFERENCES

[1] Mori, H.: Res. Rept. (1959), Lubrication Lab., Ministère de L'Air, No.334 (1957).

[2] Comolet, R.: Publications Scientifiques et Techniques du Ministère de L'Air, No.334 (1957).

[3] Hikichi, K., Togo, S., and Hioka, K.: Proc. JAST Tribology Conf. (2003) 309-310 (in Japanese).

[4] Togo, S., "Gas Bearing Design Handbook", Kyoritu-Shuppan, January 2002 (in Japanese).

[5] Epstein, A.H., "Millimeter-Scale, Micro-Electro-Mechanical Systems Gas Turbine Engines", ASME J. of Engineering for Gas Turbine and Power, Vol. 126, pp. 205-226, April 2004.

[6] Ehrich F.F., Jacobson, S.A., "Development of High-Speed Gas Bearings for High-Power Density Microdevices", ASME J. of Engineering for Gas Turbine and Power, Vol. 125, pp. 141-148, January 2003.

[7] Kang S., Johnston J.P., Arima T., Matsunaga M., Tsuru H. and Prinz F.B., ASME Turbo Expo GT2003-38933, June 2003.

[8] Peirs J., Reynaerts D. and Verplaetsen, "A Micro Gas Turbine For Electric Power Generation: Development of Turbine and Compressor", J. Micromech. Microeng. 13(5) 190-5.

[9] Salehi, M., Heshmat, H., and. Walton II, J.F., "Advancements in the Structural Stiffness and Damping of a Large Compliant Foil Journal Bearing: An Experimental Study", ASME Turbo Expo GT2004-53860, June 2004.

[10] Hikichi, K., Goto, S., Togo, S., Tanaka, S., and Isomura, K., "Hydroinertia Gas Bearings for Micro Spinners", The Fourth Int. Workshop on Micro and Nanotechnology for Power Generation and Energy Conversion Applications (PowerMEMS 2004) pp. 88-91, December 2004.

[11] Pan, C.H.T., and Malanoski, S.B., "Self-acting Bearings, Fixed Thrust Bearings, Design of Gas Bearings", Notes supplemental to the RPI-MTI course on gas bearing design, 1967.

[12] Hamrock, B.J., and Flemming, D.P., Proc. Gas Bearing Symp., University of Southampton, Paper N0.13, 1971.

[13] Flemming, D.P., and Hamrock, B.J., Proc. Gas Bearing Symp., University of Southampton, Paper N0.C1, 1974.

[14] Lund, J.W., "A Theoretical Analysis of Whirl Instability and Pneumatic Hammer for a Rigid Rotor in Pressurized Gas Journal Bearings", Trans. ASME, Journal of Lubrication Technology, pp. 154-166, April 1967.

[15] Spakovszky, Z. and Lie, L.X., "Scaling Laws for Ultra-Short Hydrostatic Gas Journal Bearings," ASME DETC2003/VIB-48468, September 2003.

[16] Spakovszky, Z., "Hydrostatic Gas Journal Bearings for Micro-Turbomachinery", 32nd Micro/ Nanomachining Seminar, Micro-rotating Machines to Support Future Mobile Machines, Tohoku University, July 2003.

[17] Mori. A., Aoyama, K., and Mori, H., "Influence of the Gas-film Inertia Forces on the Dynamic Characteristics of Externally Pressurized Gas Lubricated Journal Bearings --- Part I: Proposal of Governing Equations ---", Bulletin of JSME, Vol. 23, No. 178, April 1980.

[18] Mori. A., Aoyama, K., and Mori, H., "Influence of the Gas-film Inertia Forces on the Dynamic Characteristics of Externally Pressurized Gas Lubricated Journal Bearings --- Part II: Analyses of Whirl Instability and Plane Vibration ---", Bulletin of JSME, Vol. 23, No. 180, June 1980.